# Prediction of period doubling bifurcations in harmonically forced memristor circuits

# Prediction of period doubling bifurcations in harmonically forced memristor circuits

**Article** *in* Nonlinear Dynamics · April 2019

DOI: 10.1007/s11071-019-04847-4

CITATIONS
13

READS
195

**4 authors:**

Giacomo Innocenti
University of Florence
**79** PUBLICATIONS **736** CITATIONS
SEE PROFILE

Mauro Di Marco
Università degli Studi di Siena
**107** PUBLICATIONS **1,239** CITATIONS
SEE PROFILE

Mauro Forti
Università degli Studi di Siena
**158** PUBLICATIONS **3,965** CITATIONS
SEE PROFILE

Alberto Tesi
University of Florence
**215** PUBLICATIONS **5,821** CITATIONS
SEE PROFILE

**Nonlinear Dynamics manuscript No.**
(will be inserted by the editor)

# Prediction of Period Doubling bifurcations in harmonically forced memristor circuits

**Giacomo Innocenti · Mauro Di Marco · Mauro Forti · Alberto Tesi**

Received: ... / Accepted: ...

**Abstract** The paper studies bifurcations and complex dynamics in a class of nonautonomous oscillatory circuits with a flux-controlled memristor and harmonic forcing term. It is first shown that, as in the autonomous case, the state space of any memristor circuit of the class can be decomposed in invariant manifolds. It turns out that the memristor circuit dynamics is given by the collection of the dynamics of a family of circuits, with a nonlinear resistor in place of the memristor, which is parameterized by an additional constant input whose value depends on the initial conditions of the memristor circuit. This property makes it possible to employ the Harmonic Balance Method in order to study the periodic solutions and their bifurcations due to changing the amplitude and the frequency of the harmonic input on a fixed manifold or due to changing the initial conditions for a fixed harmonic input. The main result is that in both these cases the Harmonic Balance Method is quite effective to accurately predict period-doubling bifurcations of the periodic solutions. Analytical predictions are obtained in the cases of linear-plus-cubic and piece-wise linear memristor flux-charge characteristics.

**Keywords** Harmonic balance · Memristor · Period Doubling Bifurcation

Mauro Di Marco · Mauro Forti
Department of Information Engineering and Mathematics,
University of Siena
via Roma 56 - 53100 Siena, Italy
E-mail: {dimarco,forti}@diism.unisi.it

Giacomo Innocenti (✉) · Alberto Tesi
Department of Information Engineering,
University of Florence
via S. Marta 3 - 50139 Firenze, Italy
E-mail: {giacomo.innocenti,alberto.tesi}@unifi.it

## 1 Introduction

The first electronic implementation of the memristor (memory resistor), i.e., the fourth fundamental circuit element introduced in 1971 by Prof. Leon Chua [1], has been developed at the HP laboratories in 2008 [2]. Since then memristor devices have attracted a huge attention from researchers because they have been seen as fundamental nanoscale elements which can potentially lead to a new analogue and non-Boolean computational paradigma [3–7]. Memristor elements can indeed be exploited to build nanoscale interconnected and interacting oscillators able to display rich dynamical behaviors, including cooperative and collective dynamics [8–11].

In the last decade many contributions appeared in the literature concerning various experimental, simulative and theoretical aspects of memristors [4,5,12–15].

More specifically, an increasing interest has been addressed to memristor circuits and their extremely rich dynamical behavior. Indeed, several authors have thoroughly investigated via numerical simulations the dynamics of specific memristor circuits [16–20], as well as circuits containing other memristive devices, such as memcapacitors [21–23] and meminductors [23,24], pointing out their so-called "extreme multistability".

The peculiar mathematical property of (ideal) memristor circuits is that their state space is foliated, i.e., it amounts to a continuum of invariant manifolds where the circuit exhibits different lower-order dynamics. As an example, it is shown in [25,26] that the state space of a third-order oscillatory circuit with a single ideal memristor can be foliated in two-dimensional invariant manifolds and that the circuit dynamics is topologically equivalent to the reduced second-order dynamics on each manifolds, although the latter dynamics depends on an extra parameter that is function of the initial

conditions. The reduced dynamics is also described by a smoother vector field. The advantage is that such oscillators can be analyzed by means of known results for planar linear systems. Moreover, for Piece-Wise Linear (PWL) constitutive relations of the memristor, while the memristor circuit dynamics is described by a discontinuous vector field, the reduced dynamics is described by a continuous PWL field, preventing from the need to use the extended notion of solutions as that in the Filippov sense. The method in [26] tries to use as far as possible the standard current and voltage variables for the memristor circuit analysis. Basically the same results can be naturally obtained via a more physical approach, named Flux-Charge Analysis Method (FCAM), recently introduced in [27] as an alternative way to the standard voltage-current approach for the analysis of circuits including memristors. The use of FCAM makes it possible, as illustrated in [28] for circuits featuring a single ideal memristor, to obtain an equivalent dynamical representation in the flux-charge domain in terms of a reduced order model with an additional constant input which depends on the initial conditions of each dynamic element. Said another way, the original system in the voltage-current domain turns out to be equivalently described in the flux-charge domain via a family of reduced order systems, containing a nonlinear resistor in place of the memristor. The existence of invariant manifolds is a natural consequence of the application of FCAM and the use of the fundamental physical laws of conservation of charge or flux. This family of reduced-order systems is parameterized by an additional constant external input whose value drives the original system to different regimes, i.e., it decides the actual invariant manifold where the memristor circuit state moves on. FCAM can be naturally extended to prove in a systematic way the existence of invariant manifolds and coexisting reduced-order dynamics in a broad class of nonlinear circuits with an arbitrary number of ideal memristors [29].

This new perspective made it clear why bifurcation phenomena can be observed in a memristor circuit for fixed values of its parameters, once the initial conditions are changed. Hereafter, these phenomena will be shortly referred to as "bifurcations without parameters", just to recall they happen without varying the circuit parameters. Indeed, since the initial conditions affect the additional constant input of the reduced order model, these bifurcation phenomena can be studied by considering variations of this input. More generally, it turns out that bifurcations in memristor circuits can be investigated via standard bifurcation analysis tools applied to circuits containing nonlinear resistors in place of memristors.

Along this line of reasoning, in [30], FCAM has been applied together with the Harmonic Balance Method (HBM), which is a well-known tool for limit cycles analysis in nonlinear systems [31–33], for approximately locating periodic oscillations and their period-doubling bifurcations. More specifically, it is shown that an autonomous memristor-based Chua'a circuit can be equivalently described as a family of input-output reduced order systems with an additional external constant input, to which the HBM can be effectively applied to predict limit cycles and their period-doubling bifurcations. Also, it is pointed out how these predictions can be fruitfully exploited to locate regions where more complex dynamics should be looked for.

In this paper, a class of nonautonomous memristor oscillatory circuits forced by an external harmonic signal is considered. Indeed, several forced memristor circuits of this class have been investigated in the literature by showing a rich scenario of oscillatory and more complex behaviors as the amplitude and the frequency of the harmonic signal are varied [34–38]. Here, it is first shown that these circuits admit an equivalent input-output representation in terms of a feedback interconnection of a linear time invariant system with a static memoryless nonlinearity, subject to an external harmonic signal and an additional constant input both possibly filtered by linear time invariant systems (Section 2). As in the autonomous case, the constant input, which depends on the initial conditions of the memristor circuit, parameterizes the invariant manifolds of the space composed by the circuit state and the time. Then, the general application of the HBM to this input-output class of forced systems for predicting periodic solutions and characterizing period doubling bifurcations, is briefly outlined (Section 3). For any given frequency of the harmonic signal the predicted period doubling bifurcation curves in the harmonic amplitude and constant input plane are then computed for different nonlinear flux-charge characteristics of the memristor (Section 4). The effectiveness of the method and the accuracy of the predicted period doubling curves are discussed via some application examples, also to point out how these predicted results can be used to locate more complex behaviors via numerical simulations (Section 5).

## 2 A class of input-output models for forced memristor oscillatory circuits

In the literature, several authors have investigated the dynamical behavior of nonautonomous memristor oscillatory circuits (see, e.g., [34–38] and references therein). These papers provide very detailed analyses of complex

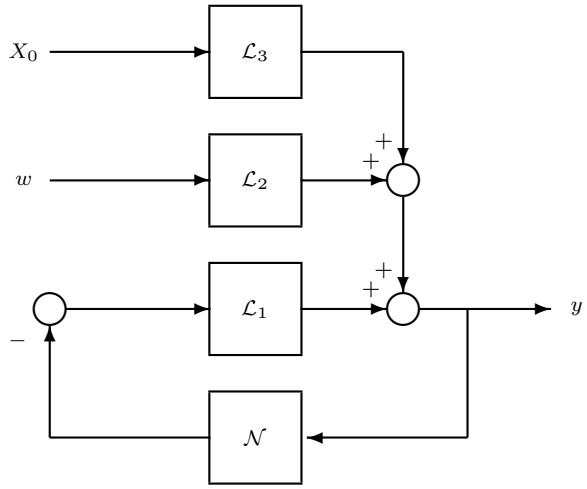


**Fig. 1** The considered class of input-output models.

behaviors and bifurcations induced by variations of the amplitude and the frequency of an external harmonic signal as well as circuit parameters. The considered circuits are basically obtained by replacing Chua's diodes or other nonlinear resistors with memristors. For instance, memristor versions of the well-known classical circuit in [39] are thoroughly considered in [34,35,37]. The many interesting complex behaviors discovered numerically and verified experimentally make it clear that memristor circuits display quite a richer complex dynamics than classical counterparts. However, a structural relation between the dynamics of classical nonlinear circuits and their memristor versions has not been provided yet. Also, a detailed investigation of how the initial conditions of memristor circuits influence their dynamical behavior has not been performed in an analytic way.

In this section we address these two issues by first showing that these memristor circuits admit the input-output representation of Fig. 1, where $\mathcal{L}_i$, $i = 1, 2, 3$, are finite dimensional linear time-invariant dynamical subsystems, $\mathcal{N}$ is a time-invariant memoryless nonlinear subsystem, $w$ is a scalar external harmonic signal of amplitude $M$, frequency $\omega_0$, and phase shift $\theta_0$, i.e., $w(\tau) = M\cos(\omega_0\tau + \theta_0)$, $X_0$ is a scalar constant input and $y$ is the scalar output. It is worth observing that the system of Fig. 1 has an internal feedback interconnection between the linear subsystem $\mathcal{L}_1$ and the nonlinear subsystem $\mathcal{N}$, while $\mathcal{L}_2$ and $\mathcal{L}_3$ are feedforward blocks driven by external harmonic and constant signals, respectively. Among the several tools developed to investigate the dynamical properties of systems enjoying this structure, the HBM has been widely used to predict periodic solutions and their bifurcations [40–46,30]. Hence, once a forced nonautonomous memristor oscillatory circuit is reduced in the form of Fig. 1, the HBM can be fruitfully used to investigate its dynamical properties.

Denoting as $\mathcal{D}$ the differential operator (i.e., $\mathcal{D}f(\tau) = \dot{f}(\tau)$), it turns out that the input-output relation of the system of Fig. 1 can be written as

$$\begin{aligned} &y(\tau) = -L_1(\mathcal{D})n(y(\tau)) \\ &+ L_2(\mathcal{D})M\cos(\omega_0\tau + \theta_0) + L_3(\mathcal{D})X_0 \ , \end{aligned} \tag{1}$$

where $n : \mathbb{R} \to \mathbb{R}$ is a static nonlinearity and $L_i(\mathcal{D})$, $i = 1, 2, 3$, are real proper rational functions of the time-derivative operator $\mathcal{D}$, i.e.:

$$L_i(\mathcal{D}) = \frac{Q_i(\mathcal{D})}{P_i(\mathcal{D})} \tag{2}$$

with $Q_i(\mathcal{D})$ and $P_i(\mathcal{D})$ denoting the numerator and the denominator of $L_i(\mathcal{D})$, respectively. Observe that relation (1) can be rewritten equivalently as

$$\begin{aligned} &P_1(\mathcal{D})P_2(\mathcal{D})P_3(\mathcal{D})y(\tau) \\ &+ Q_1(\mathcal{D})P_2(\mathcal{D})P_3(\mathcal{D})n(y(\tau)) = \\ &P_1(\mathcal{D})Q_2(\mathcal{D})P_3(\mathcal{D})M\cos(\omega_0\tau + \theta_0) \\ &+ P_1(\mathcal{D})P_2(\mathcal{D})Q_3(\mathcal{D})X_0 \ , \end{aligned} \tag{3}$$

which shows that the time domain evolution of the system of Fig. 1 is described by a nonautonomous nonlinear differential equation.

Consider the well-known Murali–Lakshmanan–Chua oscillatory memristor circuit of Fig. 2 (see, e.g., [34]). In the voltage-current domain, the time evolution of the state variables is described by the following equations

$$\begin{cases} C\dot{v}_C(t) = i_L(t) - i_M(t) \\ L\dot{i}_L(t) = -Ri_L(t) + u(t) - v_C(t) \\ \dot{\varphi}_M(t) = v_C(t) \end{cases} \tag{4}$$

which are defined for all $t \geq t_0$. The charge $q_M$ and the flux $\varphi_M$ of the memristor are related by the nonlinear flux-charge characteristic $\hat{q} : \mathbb{R} \to \mathbb{R}$, i.e.:

$$q_M = \hat{q}(\varphi_M) \ . \tag{5}$$

The memristor relation in the voltage-current domain is given by

$$i_M(t) = \hat{q}'(\varphi_M(t))v_C(t) \qquad \forall t \geq t_0, \tag{6}$$

where the derivative of the flux-charge characteristic nonlinearity, i.e. $\hat{q}'(\varphi_M(t))$, is known as the memconductance of the memristor.

The input voltage $u(t)$ is assumed to be a harmonic signal of amplitude $\hat{M}$, frequency $\hat{\omega}$, and phase shift $\hat{\theta}$, i.e.:

$$u(t) = \hat{M}\sin\left(\hat{\omega}t + \hat{\theta}\right) \qquad \forall t \geq t_0. \tag{7}$$

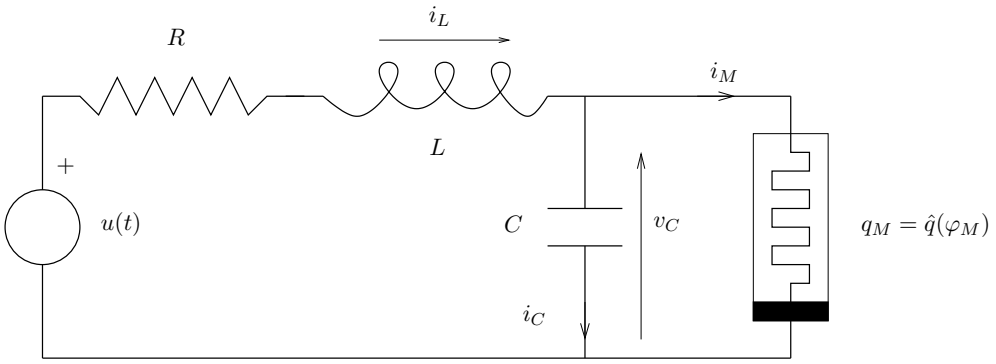


**Fig. 2** The memristive Murali–Lakshmanan–Chua circuit.

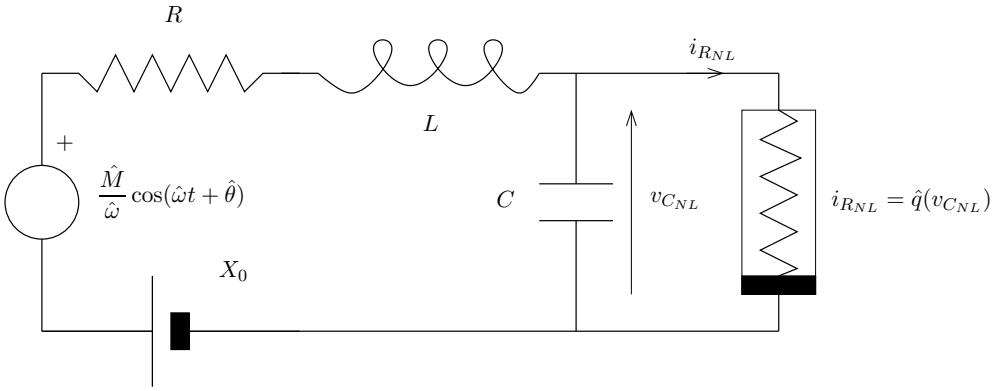


**Fig. 3** This nonlinear second-order circuit is equivalent to the third-order memristive circuit of Fig. 2 on the basis of Proposition 1. Notice that the original memristor is replaced by a nonlinear resistor, and that a new generator $X_0$ appears. This latter acts as a constant input, and so the overall dynamics turns out parametrized by its value.

This circuit shows quite a rich dynamical behavior when the amplitude $\hat{M}$ and the frequency $\hat{\omega}$ of the harmonic input and the initial conditions $v_C(t_0)$, $i_L(t_0)$, $\varphi_M(t_0)$, are varied (see, e.g., [34]). The following result provides the equivalent input-output representation (1) for the circuit (4)-(7).

**Proposition 1** *Let $L_i(\mathcal{D})$, $i = 1, 2, 3$, and $n$ be given by*

$$L_1(\mathcal{D}) = \frac{L\mathcal{D} + R}{LC\mathcal{D}^2 + RC\mathcal{D} + 1} \tag{8a}$$

$$L_3(\mathcal{D}) = \frac{1}{LC\mathcal{D}^2 + RC\mathcal{D} + 1} = -L_2(\mathcal{D}) \tag{8b}$$

*and*

$$n = \hat{q}, \tag{9}$$

*respectively, and set*

$$M = \frac{\hat{M}}{\hat{\omega}}; \qquad \omega_0 = \hat{\omega}; \qquad \theta_0 = \hat{\theta}. \tag{10}$$

*Then, the circuit* (4)-(7) *admits the equivalent input-output representation* (1) *once the output and the time variable are chosen as $y = \varphi_M$ and $\tau = t$, respectively, and the constant input $X_0$ is given by*

$$X_0 = Li_L(t_0) + RCv_C(t_0) + \varphi_M(t_0) + R\hat{q}(\varphi_M(t_0)) + \frac{\hat{M}}{\hat{\omega}}\cos(\hat{\omega}t_0 + \hat{\theta}) \ . \tag{11}$$

*Proof.* We first show that equations (4) can be rearranged in a state space form by using $x = (v_C, i_L, \varphi_M)^\top \in \mathbb{R}^3$ as the state vector. It is not difficult to show that we get

$$\begin{cases} \dot{x}(t) = Ax(t) + Bu(t) + E\sigma(t) \\ y(t) = Hx(t) \end{cases} \tag{12}$$

where the matrices $A \in \mathbb{R}^{3\times3}$, $B \in \mathbb{R}^{3\times1}$, $E \in \mathbb{R}^{3\times1}$, $H \in \mathbb{R}^{1\times3}$ are

$$A = \begin{pmatrix} 0 & \frac{1}{C} & 0 \\ -\frac{1}{L} & -\frac{R}{L} & 0 \\ 1 & 0 & 0 \end{pmatrix} \quad B = \begin{pmatrix} 0 \\ \frac{1}{L} \\ 0 \end{pmatrix} \tag{13a}$$

$$E = \begin{pmatrix} -\frac{1}{C} \\ 0 \\ 0 \end{pmatrix} \quad H = \begin{pmatrix} 0 & 0 & 1 \end{pmatrix} \tag{13b}$$

and $\sigma(t)$ is the time-derivative of $\hat{q}(\varphi_M(t))$, i.e.:

$$\sigma(t) = \mathcal{D}\hat{q}(\varphi_M(t)) \ . \tag{14}$$

Since (12) is a completely controllable and observable linear system driven by the two input signals $u(t)$ and $\sigma(t)$, its time evolution is equivalently described by the input-output relationship

$$y(t) = L_u(\mathcal{D})u(t) + L_\sigma(\mathcal{D})\sigma(t) \tag{15}$$

where

$$\begin{aligned} L_u(\mathcal{D}) &= H(\mathcal{D}I - A)^{-1}B \\ &= \frac{1}{\mathcal{D}(LC\mathcal{D}^2 + RC\mathcal{D} + 1)} \ , \end{aligned} \tag{16a}$$

$$\begin{aligned} L_\sigma(\mathcal{D}) &= H(\mathcal{D}I - A)^{-1}E \\ &= \frac{-(L\mathcal{D} + R)}{\mathcal{D}(LC\mathcal{D}^2 + RC\mathcal{D} + 1)} \ . \end{aligned} \tag{16b}$$

Hence, the output $y(t)$ and the inputs $u(t)$, $\sigma(t)$ obey to the following third order linear differential equation

$$\mathcal{D}(LC\mathcal{D}^2 + RC\mathcal{D} + 1)y(t) = u(t) - (L\mathcal{D} + R)\sigma(t) \ . \tag{17}$$

By introducing the signal

$$\begin{aligned} \hat{u}(t) &= -\mathcal{D}^{-1}u(t) = -\int_{t_0}^{t} u(\sigma)d\sigma \\ &= \frac{\hat{M}}{\hat{\omega}}\Big(\cos(\hat{\omega}t + \hat{\theta}) - \cos(\hat{\omega}t_0 + \hat{\theta})\Big) \end{aligned} \tag{18}$$

and taking into account that $y(t) = \varphi_M(t)$ and $\sigma(t) = \mathcal{D}\hat{q}(y(t))$, the differential equation (17) can be equivalently rewritten as

$$\begin{aligned} \mathcal{D}\Big[&(LC\mathcal{D}^2 + RC\mathcal{D} + 1)y(t) + \hat{u}(t) \\ &+ (L\mathcal{D} + R)\hat{q}(y(t))\Big] = 0 \ . \end{aligned} \tag{19}$$

It turns out that the differential equation (19) can be integrated by obtaining the following family of second order differential equations

$$(LC\mathcal{D}^2 + RC\mathcal{D} + 1)y(t) + \hat{u}(t) + (L\mathcal{D} + R)\hat{q}(y(t)) = K \ , \tag{20}$$

where $K$ is a constant term given by

$$\begin{aligned} K = \ &LC\mathcal{D}^2 y(t_0) + RC\mathcal{D}y(t_0) + y(t_0) \\ &+ L\mathcal{D}\hat{q}(y(t_0)) + R\hat{q}(y(t_0)) \ , \end{aligned} \tag{21}$$

where $Dy(t_0)$ stands for $Dy(t)|_{t=t_0}$, and so do all the other similar forms. To complete the proof, it is sufficient to rewrite (20) into the following equivalent form

$$y(t) = \frac{1}{LC\mathcal{D}^2 + RC\mathcal{D} + 1}\left(-(L\mathcal{D} + R)\hat{q}(y(t)) - \frac{\hat{M}}{\hat{\omega}}\cos(\hat{\omega}t + \hat{\theta}) + \frac{\hat{M}}{\hat{\omega}}\cos(\hat{\omega}t_0 + \hat{\theta}) + K\right) \tag{22}$$

and to observe that the following relations hold:

$$\begin{aligned} &y(t_0) = \varphi_M(t_0) \ , \quad \mathcal{D}y(t_0) = v_C(t_0) \ , \\ &C\mathcal{D}^2 y(t_0) + \mathcal{D}\hat{q}(y(t_0)) = i_L(t_0) \ . \end{aligned} \tag{23}$$

□

*Remark 1* It can be shown that the input-output relation provided by Proposition 1 is exactly the same pertaining to the circuit of Fig. 3, which has the same structure of the circuit of Fig. 2, with a nonlinear resistor in place of the memristor and an additional constant voltage input. Indeed, it is enough to write down the relative state equations and proceed as in the first part of the proof above. Hence, the original oscillatory memristor circuit is equivalent to a family of forced circuits containing a nonlinear resistor, whose voltage-current characteristic is given by $\hat{q}(\cdot)$. The family is parameterized by the constant input voltage $X_0$ which depends upon the initial conditions $v_C(t_0)$, $i_L(t_0)$, $\varphi_M(t_0)$ of the memristor circuit. Indeed, the proof makes it clear that, for each value of $X_0$, the manifold in the four dimensional space composed by the state vector $(v_C, i_L, \varphi_M)^\top \in \mathbb{R}^3$ and the time $t$ given by

$$\begin{aligned} \mathcal{M}_0 = \Bigg\{&(v_C, i_L, \varphi_M, t)^\top \in \mathbb{R}^4 : \ Li_L + RCv_C \\ &+ \varphi_M + R\hat{q}(\varphi_M) + \frac{\hat{M}}{\hat{\omega}}\cos(\hat{\omega}t + \hat{\theta}) = X_0\Bigg\} \end{aligned} \tag{24}$$

is invariant. This can be seen as the extension to the nonautonomous case of the well-known property of foliation of the state space of autonomous memristor circuits [27,28]. Said another way, for each $X_0$ the time behavior of the circuit of Fig. 3 is exactly equal to the time behavior of the original memristor circuit of Fig. 2 restricted to the manifold $\mathcal{M}_0$. Finally, observe that, if the flux-charge characteristic $\hat{q}(\,\cdot\,)$ is PWL, then model (4)-(6) of the memristor circuit of Figure 2 is discontinuous, while that of the circuit of Figure 3 is Lipschitz continuous.

*Remark 2* Note that $X_0$ acts as an additional parameter with respect to the circuit parameters $R$, $L$, $C$, $\hat{M}$, $\hat{\omega}$, $\hat{\phi}$ for the representation (1). According to (11), $X_0$ is fixed only if the initial conditions of the circuit are fixed. For instance, if $t_0 = 0$, $\hat{\theta} = -\pi/2$ and $v_C(t_0) = i_L(t_0) = \varphi_M(t_0) = 0$, then $X_0 = 0$ and the dynamical behavior of the memristor circuit is exactly that of the original nonlinear resistor circuit first introduced in [39]. On the other hand, qualitatively different dynamical behaviors, such as bifurcation phenomena, can be induced by varying $X_0$, i.e., by moving along the different manifolds $\mathcal{M}_0$ in (24). It turns out that $X_0$ can be varied by modifying the initial conditions $v_C(t_0)$, $i_L(t_0)$ $\varphi_M(t_0)$, while preserving constant the memristor circuit parameters. As already said in Section 1, the related bifurcation phenomena are referred to as "bifurcations without parameters" throughout the paper.

The equivalent input-output representation (1) can be devised also for other memristor circuits along the same line followed for the circuit of Fig. 2. Table 1 reports the rational functions $L_i(\mathcal{D})$, $i = 1, 2, 3$, for some circuits which have been investigated in the literature (see, e.g., [34,36,47–49], and references therein)[1]. For the circuit studied in [48], the rational function $L_2(\mathcal{D})$ is obtained once a real harmonic voltage input $(u(t) + R_s)$ is connected in parallel to the memristor (cf. Fig. 1 of [48]). For the first four circuits the memristor is flux-controlled, and hence $y = \varphi_M$ and $n = \hat{q}$, while in [49] the memristor is charge-controlled which implies $y = q_M$ and $n = \hat{\varphi}$. In all the cases expressions similar to (11) are obtained for $X_0$.

Our aim is to investigate the dynamical features of the steady-state periodic output solutions displayed by the input-output system of Fig. 1 once the constant input $X_0$ and the harmonic input amplitude $M$ and frequency $\omega_0$ are varied. In particular, we are interested in the problem of locating the set of values of $X_0$, $M$ and $\omega_0$ at which the periodic solutions undergo to some kind of bifurcations.
It is well known that this is quite a difficult task which can be in general pursued only via numerical simulations. Hence, we look for an approach which allows us to compute the sought bifurcating values of $X_0$, $M$ and $\omega_0$ in an approximate way. Indeed, we resort to the Harmonic Balance Method (HBM), which is a well-known tool for predicting steady-state periodic solutions in nonlinear systems (see [33] and references therein). Notably, it has been succesfully applied also to predict bifurcations of periodic solutions and even to locate complex attractors [40–45,30].

[1] For space limitations, $L_1(\mathcal{D})$ and $L_2(\mathcal{D})$ are expressed in terms of the related $L_3(\mathcal{D})$.

Specifically, we consider the periodic steady-state input-output relation of (1) which amounts to:

$$y(\tau) = -L_1(\mathcal{D})n(y(\tau)) + L_2(\jmath\omega_0)M\cos(\omega_0\tau + \theta_0) + L_3(0)X_0 \ , \tag{25}$$

where $y(\tau)$ and $n(y(\tau))$ are assumed to be periodic of period $\frac{2\pi}{\omega_0}$, while $L_2(\jmath\omega_0)$ and $L_3(0)$ denote the frequency gains of the rational functions $L_2(\mathcal{D})$ and $L_3(\mathcal{D})$ at $\omega_0$ and zero, respectively. To avoid degenerate cases, we assume that both $L_2(\jmath\omega_0)$ and $L_3(0)$ are bounded and not null. Also, it is assumed that $n(y(\tau))$ can be expressed in a Fourier exponential form once $y(\tau)$ is periodic.
In the next sections, it is shown how the set of couples $(X_0, M)$ at which the HBM predicts period doubling bifurcations[2], can be analytically obtained for any given frequency $\omega_0$. Also, an index to measure the accuracy of these predicted period doubling bifurcations is provided in a closed form.

## 3 Application of the HBM to the class of input-output models

We first recall the basic HBM to compute the so-called Predicted Periodic Solutions (PPSs), also providing a standard measure of their accuracy. Then, the method is applied to predict period doubling bifurcations of the PPSs.

### 3.1 Computation of PPSs via the HBM

According to the Harmonic Balance (HB) paradigma, a PPS of the following form

$$y_0(\tau) = A + B\cos(\omega_0\tau + \theta_0 - \Phi_0) = A + \frac{1}{2}Be^{\jmath(\omega_0\tau+\theta_0-\Phi_0)} + \frac{1}{2}Be^{-\jmath(\omega_0\tau+\theta_0-\Phi_0)} \tag{26}$$

is looked for to approximate the periodic solutions of period $2\pi/\omega_0$ of the system of Fig. 1. The frequency $\omega_0$ is assumed to be a given positive constant due to the periodic input, while the offset $A$, the amplitude $B$, $B > 0$, and the phase difference $\Phi_0$, $\Phi_0 \in [0, 2\pi)$, between $y_0(\tau)$ and the harmonic forcing term in (25) are unknown.
The HBM consists in first substituting the approximation (26) into (25), then balancing the continuous and the first harmonic terms, and finally solving for $A$, $B$ and $\Phi_0$ the resulting system of equations. To proceed,

[2] Similar results can be obtained for other kinds of bifurcations along the lines developed in [43].

| Circuit | $L_1(\mathcal{D})$ | $L_2(\mathcal{D})$ | $L_3(\mathcal{D})$ |
|---|---|---|---|
| [34] | $(L\mathcal{D}+R)L_3(\mathcal{D})$ | $-L_3(\mathcal{D})$ | $\frac{1}{LC\mathcal{D}^2+RC\mathcal{D}+1}$ |
| [36] | $(LRC_2\mathcal{D}^2+L\mathcal{D}+R)L_3(\mathcal{D})$ | $L_3(\mathcal{D})$ | $\frac{1}{LRC_1C_2\mathcal{D}^3+L(C_1+C_2)D^2+RC_1\mathcal{D}+1}$ |
| [47] | $L\mathcal{D}L_3(\mathcal{D})$ | $\frac{L}{R}L_3(\mathcal{D})$ | $\frac{R}{LRC\mathcal{D}^2-L\mathcal{D}+R}$ |
| [48] | $\frac{R_s(R_2-R_1R_3C_1\mathcal{D})}{R_2}L_3(\mathcal{D})$ | $\frac{R_2-R_1R_3C_1\mathcal{D}}{R_2}L_3(\mathcal{D})$ | $\frac{R_2}{R_sR_2C_1C_2\mathcal{D}^2+(R_sR_2(C_1+C_2)-R_1R_3C_1)\mathcal{D}+R_2}$ |
| [49] | $C\mathcal{D}L_3(\mathcal{D})$ | $CL_3(\mathcal{D})$ | $\frac{1}{LC\mathcal{D}^2+1}$ |

**Table 1** Input-output equivalent description of forced memristive circuits.

let us express $n(y_0(\tau))$ in its Fourier exponential form, i.e.:

$$n(y_0(\tau)) = \sum_{h=-\infty}^{\infty} p_h e^{\jmath h\omega_0\tau} \ , \tag{27}$$

where

$$p_h = \frac{1}{2\pi}\int_{-\pi}^{\pi} n(y_0(\tau))e^{-\jmath h\omega_0\tau}d\omega_0\tau \quad h=0,1,\dots \tag{28}$$

and $p_{-h} = p_h^\star$, $h = 1,2,\dots$, with the star operator standing for complex conjugate. In particular, by introducing the standard nonlinear HB gains reported in Table 2 it turns out that (27) can rewritten as

$$\begin{aligned} n(y_0(\tau)) &= N_0(A,B)A \\ &+ \frac{1}{2}N_1^\star(A,B)Be^{-\jmath(\omega_0\tau+\theta_0-\Phi_0)} \\ &+ \frac{1}{2}N_1(A,B)Be^{\jmath(\omega_0\tau+\theta_0-\Phi_0)} \\ &+ \sum_{h=2}^{+\infty}\left(p_h^\star(A,B)e^{-\jmath h\omega_0\tau} + p_h(A,B)e^{\jmath h\omega_0\tau}\right) \ , \end{aligned} \tag{30}$$

thus making explicit the constant and the first harmonic terms as well as the dependence of $p_h$ from $A$ and $B$. Now, substituting (26) and (30) into (25) and considering the steady-state periodic outputs of the linear subsystems $\mathcal{L}_1$ of Fig. 1, restricted to the constant and first harmonic terms, we get the following relation:

$$\begin{aligned} &A + \frac{1}{2}Be^{-\jmath(\omega_0\tau+\theta_0-\Phi_0)} + \frac{1}{2}Be^{\jmath(\omega_0\tau+\theta_0-\Phi_0)} \\ &= -L_1(0)N_0(A,B)A \\ &- \frac{1}{2}L_1(-\jmath\omega_0)N_1^\star(A,B)Be^{-\jmath(\omega_0\tau+\theta_0-\Phi_0)} \\ &- \frac{1}{2}L_1(\jmath\omega_0)N_1(A,B)Be^{\jmath(\omega_0\tau+\theta_0-\Phi_0)} \\ &+ \frac{1}{2}L_2(-\jmath\omega_0)Me^{-\jmath(\omega_0\tau+\theta_0)} \\ &+ \frac{1}{2}L_2(\jmath\omega_0)Me^{\jmath(\omega_0\tau+\theta_0)} + L_3(0)X_0 \ . \end{aligned} \tag{31}$$

Hence, by balancing the continuous terms in (31) we get the real equation

$$A\left(1+L_1(0)N_0(A,B)\right) = L_3(0)X_0 \ , \tag{32}$$

while balancing the first harmonic terms we obtain the complex equation

$$B\left(1+L_1(\jmath\omega_0)N_1(A,B)\right) = L_2(\jmath\omega_0)e^{\jmath\Phi_0}M \ . \tag{33}$$

Equations (32)-(33) are the well-known HB equations which have to be solved for $A$, $B$ and $\Phi_0$ to obtain the PPSs (26) for given $\omega_0$, $M$, $X_0$.

For the development of next Proposition 2, it is important to note that for given constant $A$, amplitude $B$ and frequency $\omega_0$, the corresponding values of $X_0$, $M$ and $\Phi_0$ ensuring the solution of (32)-(33) are readily obtained as

$$\begin{aligned} X_0 &= \frac{A}{L_3(0)}\left(1+L_1(0)N_0(A,B)\right) \\ &= X_0(A,B) \ , \end{aligned} \tag{34}$$

$$\begin{aligned} M &= B\frac{|1+L_1(\jmath\omega_0)N_1(A,B)|}{|L_2(\jmath\omega_0)|} \\ &= M(A,B,\omega_0) \ , \end{aligned} \tag{35}$$

$$\begin{aligned} \Phi_0 &= \arg\left\{\frac{B\left(1+L_1(\jmath\omega_0)N_1(A,B)\right)}{L_2(\jmath\omega_0)M(A,B,\omega_0)}\right\} \\ &= \Phi_0(A,B,\omega_0) \ . \end{aligned} \tag{36}$$

Note that the first two equations above provide the values of the constant input $X_0$ and of the amplitude $M$ of the harmonic term which are compatible with a PPS of type (26), while the third equation provides the corresponding admissible values of phase difference $\Phi_0$.

The problem of accuracy of the PPSs has been investigated since long time, also providing conditions for the existence of a true periodic solution close to the predicted one (see [33] and references therein). A requirement at the basis of these conditions is that $L_1(s)$ is a low-pass filter and the nonlinearity $n(\cdot)$ does not

$$N_0(A,B) = \frac{1}{2\pi A}\int_{-\pi}^{\pi} n(A + B\cos(\omega_0\tau))d\omega_0\tau \tag{29a}$$

$$N_1(A,B) = \frac{1}{\pi B}\int_{-\pi}^{\pi} n(A + B\cos(\omega_0\tau))e^{-\jmath\omega_0\tau}d\omega_0\tau \tag{29b}$$

**Table 2** Nonlinear HB gains of $n(\cdot)$.

generate large higher-order harmonics. A quantitative measure of the accuracy of a PPS is the so-called *distortion index*, which is defined as [31]

$$D(A,B,\omega_0) = \frac{\|\tilde{y}_0(\tau) - y_0(\tau)\|_2}{\|y_0(\tau)\|_2} \tag{37}$$

where $\|\cdot\|_2$ denotes the standard $L_2$-norm of periodic signals and $\tilde{y}_0(\tau)$ is the (steady-state) periodic output of the system (25) of Fig. 1 once the input of $n(\cdot)$ is assumed to be exactly equal to the PPS $y_0(\tau)$ in (26), i.e., exploiting (31):

$$\begin{aligned}\tilde{y}_0(\tau) = &-L_1(0)N_0(A,B)A\\ &-\frac{1}{2}L_1(-\jmath\omega_0)N_1^\star(A,B)Be^{-\jmath(\omega_0\tau+\theta_0-\Phi_0)}\\ &-\frac{1}{2}L_1(\jmath\omega_0)N_1(A,B)Be^{\jmath(\omega_0\tau+\theta_0-\Phi_0)}\\ &-\sum_{h=2}^{\infty}\Big(L_1(-\jmath h\omega_0)p_h^\star(A,B)e^{-\jmath h\omega_0\tau}\\ &+L_1(\jmath h\omega_0)p_h(A,B)e^{\jmath h\omega_0\tau}\Big)\\ &+\frac{1}{2}L_2(-\jmath\omega_0)Me^{-\jmath(\omega_0\tau+\theta_0)}\\ &+\frac{1}{2}L_2(\jmath\omega_0)Me^{\jmath(\omega_0\tau+\theta_0)} + L_3(0)X_0\ .\end{aligned} \tag{38}$$

It is not difficult to verify that $D(A,B,\omega_0)$ admits the following expression

$$D(A,B,\omega_0) = \sqrt{\frac{\sum_{h=2}^{\infty} 2|L_1(\jmath h\omega_0)|^2|p_h(A,B)|^2}{A^2 + B^2/2}} \tag{39}$$

where $p_h$, $h = 2,3,\ldots$, are computed according to (28) and clearly depend on the actual values of $A$ and $B$ of the PPS. Obviously, the accuracy of the PPS increases as $D(A,B,\omega_0)$ decreases to zero.

### 3.2 Characterization of period doubling bifurcations via the HBM

The HBM has been applied to predict bifurcations in nonlinear systems since long time [40–43]. In particular, for the case of period doubling bifurcations, the HBM assumes that the nominal solution (26) is perturbed as follows

$$y(\tau) = \ y_0(\tau) + \delta y(\tau)\ , \tag{40}$$

where $y_0(\tau)$ is the PPS solving the HB equations (32))-(33) and $\delta y(\tau)$ is a small periodic perturbation which represents the birth of the subharmonic term generated by a period doubling bifurcation. Therefore, the HBM considers the perturbation

$$\delta y(\tau) = \varepsilon\cos\Big(\frac{\omega_0}{2}\tau + \theta_0 - \Phi_0 + \psi_0\Big)\ , \tag{41}$$

where $\varepsilon$ is a small positive constant and $\psi_0$ represents the phase difference between $y_0(\tau)$ and $\delta y(\tau)$.
Clearly, the perturbed periodic solution (40) has twice the period of the PPS $y_0(t)$. The bifurcation condition in the HB approach is obtained by imposing that $y(\tau)$ is a solution of (25) and then balancing the constant term and the harmonic terms at $\omega_0$ and $\omega_0/2$ by letting $\varepsilon$ tending to zero.
Observing that

$$n(y_0 + \delta y) = n(y_0) + n'(y_0)\delta y + \ldots\ , \tag{42}$$

the application of the HBM to (25) yields the following equation:

$$\begin{aligned}&y_0(\tau) + \delta y(\tau) = -L_1(\mathcal{D})n(y_0(\tau))\\ &+ L_2(\jmath\omega_0)M\cos(\omega_0\tau + \theta_0) + L_3(0)X_0\\ &- L_1(\mathcal{D})n'(y_0)\delta y(\tau) + \ldots\ .\end{aligned} \tag{43}$$

Clearly, since $\delta y(\tau)$ is small ($\varepsilon$ goes to zero), equating the constant terms and the harmonic terms at frequency $\omega_0$ of (43) leads to equations (32)-(33). Then, the additional condition characterizing the period doubling bifurcation is obtained by balancing the harmonic terms at frequency $\omega_0/2$ of the remaining equation:

$$\delta y(\tau) = \ -L_1(\mathcal{D})n'(y_0(\tau))\delta y(\tau)\ . \tag{44}$$

To this aim, note that $n'(y_0(\tau))$ is periodic of period $2\pi/\omega_0$ and thus it admits an exponential Fourier representation containing the continuous term and the harmonic term at frequency $\omega_0$.

$$F_0(A,B) = \frac{1}{2\pi}\int_{-\pi}^{\pi} n'(A + B(\cos\omega_0\tau))d\omega_0\tau \tag{45a}$$

$$F_1(A,B) = \frac{1}{2\pi}\int_{-\pi}^{\pi} n'(A + B(\cos\omega_0\tau))e^{-\jmath\omega_0\tau}d\omega_0\tau \ , \tag{45b}$$

**Table 3** Nonlinear HB gains of $n'(\cdot)$.

Then, by introducing the HB gains in Table 3 and taking into account that both sides of equation (44) are linear in $\varepsilon$, it can be shown that that the sought HB period doubling equation amounts to

$$1 + L_1\left(\jmath\frac{\omega_0}{2}\right)\left(F_0(A,B) + F_1(A,B)e^{-\jmath 2\psi_0}\right) = \ 0 \ , \tag{46}$$

where, to avoid degenerate cases, $L_1\left(\jmath\frac{\omega_0}{2}\right)$ is assumed to be bounded and not null.
In the HB approach, if the offset $A$ and the amplitude $B$ of a PPS are such that there exists $\psi_0$ solving the complex equation (46), then the PPS is said to undergo to a Predicted Period Doubling (PPD) bifurcation at $\varepsilon = 0$. Hence, for any given frequency $\omega_0$, PPD bifurcation points in the $(X_0, M)$-plane are obtained by first computing the couples $(A, B)$ which solve (46) for suitable $\psi_0$ and then substituting the found couples into equations (34)-(35). The corresponding values of $X_0$ and $M$ provide the sought PPD bifurcation points in the $(X_0, M)$-plane.

## 4 Predicted Period Doubling (PPD) bifurcations in the class of input-output models

In this section we show how the PPD bifurcation points can be computed. We first consider the case of a general nonlinearity $n(\cdot)$, while linear-plus-cubic and PWL nonlinearities are dealt with in subsection 4.1 and 4.2, respectively.
The complex equation (46) can be split into two real equations, one for the phase and the other for the magnitude. The phase equation amounts to

$$\begin{aligned}\psi^0 &= -\frac{1}{2}\arg\left\{-\frac{L_1^{-1}\left(\jmath\frac{\omega_0}{2}\right) + F_0(A,B)}{F_1(A,B)}\right\} \\ &= \psi^0(A,B,\omega_0) \ ,\end{aligned} \tag{47}$$

and it provides the perturbation phase shift as a function of the forcing frequency $\omega_0$ and the offset $A$ and amplitude $B$ of PPS. The magnitude equation, instead, reads

$$\left|L_1^{-1}\left(\jmath\frac{\omega_0}{2}\right) + F_0(A,B)\right| = \ |F_1(A,B)| \ , \tag{48}$$

and it represents, for any given $\omega_0$, a condition which every couple $(A, B)$ must satisfy for the PPD bifurcation to happen. Now, let us introduce the following set

$$\begin{aligned}\mathcal{S}_{\omega_0} = \Big\{ & A \in \mathbb{R}, B \in \mathbb{R}^+ : \\ & \left|L_1^{-1}\left(\jmath\frac{\omega_0}{2}\right) + F_0(A,B)\right| = |F_1(A,B)|\Big\},\end{aligned} \tag{49}$$

i.e., the set of all couples of $(A, B)$ solving (48) for a given $\omega_0$. The following result pertains to $\mathcal{S}_{\omega_0}$.

**Proposition 2** *The PPS $y_0(\tau)$ in (26) undergoes to a PPD if and only if the corresponding offset $A$ and amplitude $B$ are such that*

$$(A,B) \in \mathcal{S}_{\omega_0} \ . \tag{50}$$

*Moreover, the PPD bifurcation manifold in the $(X_0, M)$-plane is given by*

$$\begin{aligned}\mathcal{M}_{X_0,M} = \big\{ & (X_0, M) : \ X_0 = X_0(A,B), \\ & M = M_0(A,B,\omega_0), \ (A,B) \in \mathcal{S}_{\omega_0}\big\}\end{aligned} \tag{51}$$

*where $X_0(A, B)$ and $M_0(A, B, \omega_0)$ are as in (34)-(35), respectively.*

*Proof.* The proof readily follows by observing that the PPS $y_0(\tau)$ exists if and only if $A$, $B$, $\omega_0$ are such that $X_0 = X_0(A, B)$, $M = M_0(A, B, \omega_0)$, $\Phi_0 = \Phi_0(A, B, \omega_0)$ (see (36)) and it undergoes to a PPD if and only if $A$, $B$, $\omega_0$ are such that (50) holds. □

*Remark 3* The above Proposition makes it clear that PPD bifurcations exist if and only if the one-dimensional manifold $\mathcal{S}_{\omega_0}$ is not empty. Said another way, PPD bifurcations are completely characterized once the set $\mathcal{S}_{\omega_0}$ is obtained. In general, computing $\mathcal{S}_{\omega_0}$ amounts to solving a nonlinear equation in two unknowns. This clearly means that $\mathcal{S}_{\omega_0}$ is in general a one-dimensional set.

*Remark 4* Note that the PPD bifurcation manifold in the $(X_0, M)$-plane is directly obtained as the image of $\mathcal{S}_{\omega_0}$ via relations (34)-(35). Also, observe that for small values of $\varepsilon$ the corresponding nearly bifurcated periodic solutions (40)-(41) are obtained once $\Phi_0$ and $\psi_0$ are found by (36) and (47), respectively.

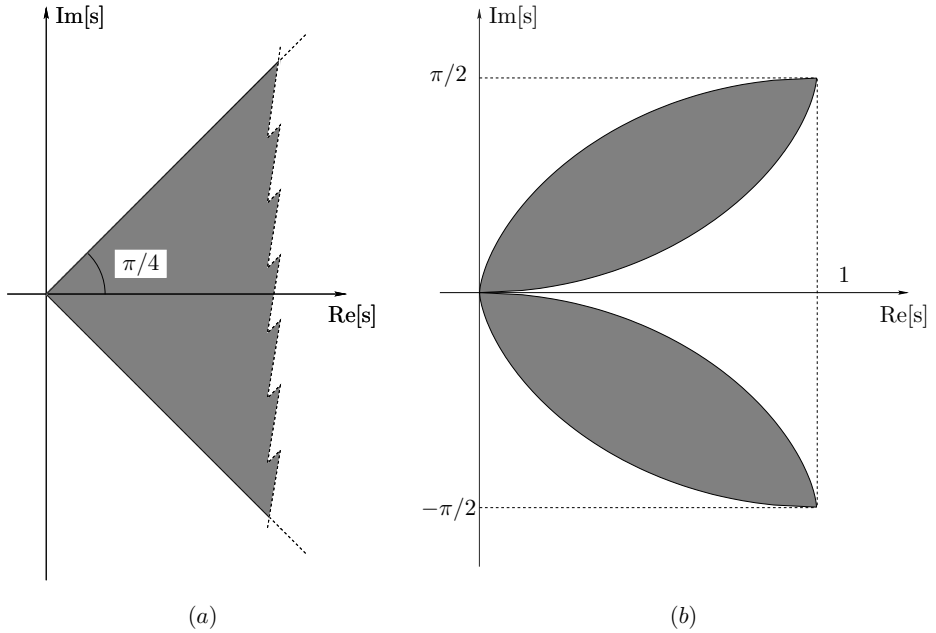


**Fig. 4** Graphical interpretation of PPD bifurcation manifold in the $(X_0, M)$ space. a) Conditions (59) and (60) for nonlinearity (52). b) Condition (83) for nonlinearity (73).

*Remark 5* The PPD bifurcation manifold in the three-dimensional $(X_0, M, \omega_0)$ space can be computed by collecting the two-dimensional sets (51) generated by all the non-empty sets $\mathcal{S}_{\omega_0}$. For the nonlinearities considered in the next subsections, it will be shown that the intervals of $\omega_0$ such that $\mathcal{S}_{\omega_0} \not\equiv \emptyset$ can be readily singled out.

### 4.1 Predicted Period Doubling (PPD) bifurcations: linear plus cubic case

In this subsection we assume that the nonlinear function $n(\cdot)$ in (25) has the following form

$$n(y) = m_0 y + m_1 y^3 \ , \tag{52}$$

where $m_0$ and $m_1$ are given constants such that $m_1 \neq 0$. The HB gains $N_0$, $N_1$ in (29) and $F_0$, $F_1$ in (45) turn out to have the following expressions:

$$N_0(A,B) = m_0 + m_1 A^2 + \frac{3}{2} m_1 B^2 \ , \tag{53a}$$

$$N_1(A,B) = m_0 + 3m_1 A^2 + \frac{3}{4} m_1 B^2 \ , \tag{53b}$$

$$F_0(A,B) = m_0 + 3m_1 A^2 + \frac{3}{2} m_1 B^2 \ , \tag{53c}$$

$$F_1(A,B) = 3m_1 AB \ . \tag{53d}$$

Then, equations (47) and (48) boil down to

$$\psi^0(\omega_0, A, B) = -\frac{1}{2} \arg \left\{ -\frac{m_0}{3m_1 AB} - \frac{1}{3m_1 AB} L_1^{-1}\left(\jmath \frac{\omega_0}{2}\right) - \frac{A}{B} - \frac{B}{2A} \right\} \ , \tag{54}$$

$$|3m_1 AB| = \left| L_1^{-1}\left(\jmath \frac{\omega_0}{2}\right) + m_0 + 3m_1 A^2 + \frac{3}{2} m_1 B^2 \right| \ , \tag{55}$$

respectively. As already underlined, equation (54) provides $\psi^0$ and it only serves to get the bifurcated periodic solution approximation. Equation (55), instead, characterizes the set $\mathcal{S}_{\omega_0}$ according to Proposition 2. To obtain this set, it is convenient to rewrite (55) as

$$|3m_1 AB| = \left| -m_1 \alpha(\omega_0) - \jmath m_1 \beta(\omega_0) + 3m_1 A^2 + \frac{3}{2} m_1 B^2 \right| \ , \tag{56}$$

where

$$\alpha(\omega_0) = -\frac{\mathrm{Re}\left[L_1^{-1}\left(\jmath\frac{\omega_0}{2}\right)\right] + m_0}{m_1} \tag{57}$$

and

$$\beta(\omega_0) = -\frac{\mathrm{Im}\left[L_1^{-1}\left(\jmath\frac{\omega_0}{2}\right)\right]}{m_1} \tag{58}$$

are constants for a given $\omega_0$. Note that $\alpha(\omega_0)$ and $\beta(\omega_0)$ depends on the gain of the rational transfer function $L_1(s)$ at $s = \jmath\omega_0/2$ and the constants $m_0$ and $m_1$ of the nonlinear function (52).

The following result provides an analytic description of the set $\mathcal{S}_{\omega_0}$.

**Proposition 3** *If conditions*

$$|\alpha(\omega_0)| \geq |\beta(\omega_0)| \tag{59}$$

*and*

$$\alpha(\omega_0) > 0 \tag{60}$$

*hold, then*

$$\mathcal{S}_{\omega_0} = \Bigg\{ A \in \mathbb{R},\ B \in \mathbb{R}^+ :\ \left(A^2 - k(\omega_0)\right)^2 + \left(\frac{B^2}{2} - k(\omega_0)\right)^2 = h^2(\omega_0) \Bigg\}, \tag{61}$$

*where*

$$k(\omega_0) = \frac{\alpha(\omega_0)}{3} \tag{62}$$

$$h(\omega_0) = \frac{\sqrt{\alpha^2(\omega_0) - \beta^2(\omega_0)}}{3}\ . \tag{63}$$

*Otherwise, $\mathcal{S}_{\omega_0}$ is empty.*

*Proof.* By making the squares of (56) we get the equivalent relation

$$9m_1^2A^2B^2 = \left(-m_1\alpha(\omega_0) + 3m_1A^2 + \frac{3}{2}m_1B^2\right)^2 + m_1^2\beta^2(\omega_0) \tag{64}$$

which, since $m_1 \neq 0$, can be rearranged as

$$9\left(A^2 - \frac{\alpha(\omega_0)}{3}\right)^2 + \frac{9}{4}\left(B^2 - \frac{2\alpha(\omega_0)}{3}\right)^2 = \alpha^2(\omega_0) - \beta^2(\omega_0)\ . \tag{65}$$

Hence, if condition (59) does not hold, then equation (65) has no solutions, implying that the set $\mathcal{S}_{\omega_0}$ is empty. If condition (59) holds, then (65) can be rewritten in the following equivalent form

$$\left(A^2 - k(\omega_0)\right)^2 + \left(\frac{B^2}{2} - k(\omega_0)\right)^2 = h^2(\omega_0)\ , \tag{66}$$

where $k(\omega_0)$ and $h(\omega_0)$ are as in (62) and (63), respectively. Now, equation (66) describes a circle of center $(k(\omega_0), k(\omega_0))$ and radius $h(\omega_0)$ in the $(A^2, \frac{B^2}{2})$-plane. Moreover, since the radius $h(\omega_0)$ is not larger than the absolute value of the center $k(\omega_0)$, it turns out that the circle entirely lies in a quadrant of the plane. Hence, the set $\mathcal{S}_{\omega_0}$ is not empty if and only if the center belongs to the positive quadrant, i.e., if and only if condition (59)-(60) hold. □

*Remark 6* The proof makes it clear that the set $\mathcal{S}_{\omega_0}$ either it is empty or it is composed of two closed curves which can be described parametrically as

$$\Big\{A, B :\ A = A(\lambda) = \pm\sqrt{k(\omega_0) + h(\omega_0)\cos(\lambda)},\ B = B(\lambda) = \sqrt{2k(\omega_0) + 2h(\omega_0)\sin(\lambda)},\ \lambda \in [0, 2\pi)\Big\}. \tag{67}$$

Note the two curves are symmetric in the $(A, B)$-plane with respect to the $B$-axis. Also, if $h(\omega_0) = 0$ the two curves collapse to two single points.

Proposition 3 allows for the next analytical characterization of the PPD bifurcation manifold $\mathcal{M}_{X_0,M}$.

**Proposition 4** *Let conditions* (59) *and* (60) *hold. Then, $\mathcal{M}_{X_0,M}$ in* (51) *is given once*

$$X_0(A, B) = L_3^{-1}(0)\left(1 + L_1(0)\left(m_1A^2 + m_0 + \frac{3}{2}m_1B^2\right)\right)A\ , \tag{68}$$

$$M(A, B, \omega_0) = \frac{\left|1 + L_1(\jmath\omega_0)(m_0 + 3m_1A^2 + \frac{3}{4}m_1B^2)\right| B}{|L_2(\jmath\omega_0)|} \tag{69}$$

*and $(A, B) \in \mathcal{S}_{\omega_0}$.*

*Proof.* The proof directly follows from Proposition 2 once the expressions of $N_0$ and $N_1$ in (53) are substituted in (34) and (35), respectively. □

*Remark 7* By substituting the expressions $A(\lambda)$ and $B(\lambda)$ of (67) into (68) and (69), we get an analytical representation of $\mathcal{M}_{X_0,M}$ in terms of two closed curves (possibly collapsing into two single points if $h(\omega_0) = 0$) in the $(M, X_0)$-plane, which are parameterized by $X_0(\lambda)$ and $M(\lambda)$ for $\lambda \in [0, 2\pi)$. Note that the two curves are generated by assuming $A(\lambda) = -|A(\lambda)|$ and $A(\lambda) = |A(\lambda)|$ and thus, from (68)-(69), it turns out that the two curves have the same value for $M(\lambda)$ while opposite values for $X_0(\lambda)$. Said another way, the two curves are symmetric with respect the $M$-axis.

*Remark 8* Observe that the existence of these two PPD bifurcation curves is ensured by conditions (59) and (60), which have a simple geometrical interpretation in the complex plane (see Fig. 4.a). Indeed, if we consider the region of the complex plane

$$S_{lc} = \left\{ s \in \mathbb{C} : \ |\arg s| \leq \frac{\pi}{4} \right\} , \tag{70}$$

then (59) and (60) are satisfied if and only if

$$-\frac{L_1^{-1}\left(\jmath\frac{\omega_0}{2}\right) + m_0}{m_1} \in S_{lc} . \tag{71}$$

It is worth noting that (71) only depends on the gain at $s = \jmath\omega_0/2$ of the transfer function $L_1(s)$ and on the parameters $m_0$ and $m_1$ of the nonlinearity 52. Moreover, the intervals of $\omega_0$ such that $\mathcal{S}_{\omega_0} \not\equiv \emptyset$ can be readily computed via the graphical condition (71). According to Remark 5, this permits to obtain the PPD bifurcation manifold in the three-dimensional $(X_0, M, \omega_0)$-space.

*Remark 9* The accuracy of the PPD bifurcation curves can be evaluated by computing the distortion index $D(A, B, \omega_0)$ in (39). It turns out that only $p_2$ and $p_3$ are non-zero and indeed we get

$$D(A, B, \omega_0) = \sqrt{\frac{\frac{9}{8}m_1^2A^2B^4|L_1(\jmath 2\omega_0)|^2 + \frac{1}{32}m_1^2B^6|L_1(\jmath 3\omega_0)|^2}{A^2 + \frac{B^2}{2}}} , \tag{72}$$

which shows that in general the accuracy of PPSs is higher when $|L_1(\jmath 2\omega_0)|$, $|L_1(\jmath 3\omega_0)|$ and $m_1$ are small, thus ensuring the well-known filtering hypothesis along the internal feedback loop of the system of Fig. 1 [31]. Note that, once the expressions $A(\lambda)$ and $B(\lambda)$ of (67) are substituted into (72), the value $D(A(\lambda), B(\lambda), \omega_0)$ provides a measure of the accuracy of the corresponding PPD bifurcation point $(X_0(A(\lambda), B(\lambda)), M(A(\lambda), B(\lambda))$ in the $(M, X_0)$-plane.

### 4.2 Predicted Period Doubling (PPD) bifurcations: PWL case

In this subsection we assume that the nonlinear function $n(\cdot)$ in (25) is PWL. Moreover, we consider the following nonlinearity

$$n(y) = \begin{cases} m_0 y & \text{if } y \leq 1 \\ m_0 + m_1(y-1) & \text{if } y > 1 \end{cases} , \tag{73}$$

where the constants $m_0$ and $m_1$ are such that $m_1 \neq m_0$. Clearly, the PPSs of interest are those containing inside their range the point $y = 1$, which implies that $A$ and $B$ are such that $|1 - A| \leq B$. Under this assumption, the gains $N_0$, $N_1$ in (29) and $F_0$, $F_1$ in (45) turn out to have the expressions reported in Table 4.

To obtain the set $\mathcal{S}_{\omega_0}$ of Proposition 2, we observe that (48) boils down to

$$\sqrt{1 - \left(\frac{1-A}{B}\right)^2} = \left| \bar{\alpha}(\omega_0) + \jmath\bar{\beta}(\omega_0) - \arccos\left(\frac{1-A}{B}\right) \right| , \tag{78}$$

where

$$\bar{\alpha}(\omega_0) = -\frac{\pi}{m_1 - m_0}\left(\mathrm{Re}\left[L_1^{-1}\left(\jmath\frac{\omega_0}{2}\right)\right] + m_0\right) \tag{79}$$

and

$$\bar{\beta}(\omega_0) = -\frac{\pi}{m_1 - m_0}\mathrm{Im}\left[L_1^{-1}\left(\jmath\frac{\omega_0}{2}\right)\right] \tag{80}$$

are constants for any given $\omega_0$. By introducing the phase variable

$$\bar{\theta} = \arccos\left(\frac{1-A}{B}\right) , \tag{81}$$

equation (78) can be equivalently rewritten as an equation involving only $\bar{\theta}$, i.e.:

$$\sin^2\bar{\theta} = (\bar{\theta} - \bar{\alpha}(\omega_0))^2 + \bar{\beta}^2(\omega_0) . \tag{82}$$

$$N_0(A,B) = m_0 - \frac{m_1-m_0}{\pi A}\left((1-A)\arccos\left(\frac{1-A}{B}\right) - B\sqrt{1-\left(\frac{1-A}{B}\right)^2}\right) \tag{74}$$

$$N_1(A,B) = m_0 - \frac{m_1-m_0}{\pi B}\left((1-A)\sqrt{1-\left(\frac{1-A}{B}\right)^2} - B\arccos\left(\frac{1-A}{B}\right)\right) \tag{75}$$

$$F_0(A,B) = m_0 + \frac{m_1-m_0}{\pi}\arccos\left(\frac{1-A}{B}\right) \tag{76}$$

$$F_1(A,B) = \frac{m_1-m_0}{\pi}\sqrt{1-\left(\frac{1-A}{B}\right)^2} \tag{77}$$

**Table 4** Nonlinear HB gains for nonlinearity (73).

Hence, the computation of the set $\mathcal{S}_{\omega_0}$ is reduced to solve (82) for $\bar\theta \in [0,\pi]$ and then to recover the corresponding values of $A$ and $B$ from (81). Indeed, we have the following result.

**Proposition 5** *If condition*

$$\left|\bar\alpha(\omega_0) - \arcsin\sqrt{|\bar\beta(\omega_0)|}\right| \leq \sqrt{|\bar\beta(\omega_0)|}\sqrt{1-|\bar\beta(\omega_0)|} \tag{83}$$

*holds, then*

$$\mathcal{S}_{\omega_0} = \left\{A\in\mathbb{R}, B\in\mathbb{R}^+ :\ A + B\cos\bar\theta_1 - 1 = 0\right\} \bigcup \left\{A\in\mathbb{R}, B\in\mathbb{R}^+ :\ A + B\cos\bar\theta_2 - 1 = 0\right\}, \tag{84}$$

*where $\bar\theta_1$ and $\bar\theta_2$ are the two solutions of* (82)*. Otherwise, $\mathcal{S}_{\omega_0}$ is empty.*

*Proof.* We first observe that if (82) is solved for some $\bar\theta$ then $\left\{A\in\mathbb{R}, B\in\mathbb{R}^+ :\ A + B\cos\bar\theta - 1 = 0\right\} \in \mathcal{S}_{\omega_0}$. Hence, to prove (84) it is enough to show that if (83) holds then (82) admits two solutions, while no solutions exist if (83) does not hold.
It turns out that any solution $\bar\theta$ of (82) can be obtained as the intersection of the following two functions

$$\begin{aligned} f(\bar\theta) &= \bar\theta^2 - \sin^2\bar\theta\ , \\ l(\bar\theta) &= 2\bar\alpha(\omega_0)\bar\theta - \bar\alpha^2(\omega_0) - \bar\beta^2(\omega_0)\ . \end{aligned} \tag{85}$$

Since $f(\bar\theta)$ is a nonnegative nondecreasing function and $l(\bar\theta)$ is an affine linear function such that $f(0) \geq l(0)$ and $f(\pi) > l(\pi)$ for all $\bar\alpha(\omega_0)$ and $\bar\beta(\omega_0)$, it turns out that $f(\bar\theta)$ and $l(\bar\theta)$ have either two intersections or no intersections. More specifically, there exist two distinct intersections if and only if $l(\bar\theta) > f(\bar\theta)$ for some $\bar\theta \in (0,\pi)$ and two coincident intersections if $f(\bar\theta)$ and $l(\bar\theta)$ are tangent. By imposing the tangency condition between $f(\bar\theta)$ and $l(\bar\theta)$, we get

$$2\bar\theta - 2\sin\bar\theta\cos\bar\theta = \ 2\bar\alpha(\omega_0)$$

and, from (82),

$$\sin^2\bar\theta = \ \sin^2\bar\theta\cos^2\bar\theta + \bar\beta^2(\omega_0)\ ,$$

which boils down to

$$\sin^4\bar\theta = \ \bar\beta^2(\omega_0)\ .$$

Hence, $f(\bar\theta)$ and $l(\bar\theta)$ are tangent at $\bar\theta = \bar\theta^\star$, with

$$\bar\theta^\star = \arcsin\sqrt{|\bar\beta(\omega_0)|}\ ,$$

if and only $|\bar\beta(\omega_0)| \leq 1$ and

$$\bar\alpha(\omega_0) = \begin{cases} \bar\alpha_+(\omega_0) = \arcsin\sqrt{|\bar\beta(\omega_0)|} \\ \qquad\qquad +\sqrt{|\bar\beta(\omega_0)|}\sqrt{1-|\bar\beta(\omega_0)|} \\ \bar\alpha_-(\omega_0) = \arcsin\sqrt{|\bar\beta(\omega_0)|} \\ \qquad\qquad -\sqrt{|\bar\beta(\omega_0)|}\sqrt{1-|\bar\beta(\omega_0)|} \end{cases}\ . \tag{86}$$

Observe that the following relations

$$\begin{aligned} l(\bar\theta^\star) &= 2\bar\alpha_-(\omega_0)\bar\theta^\star - \bar\alpha_-^2(\omega_0) - \bar\beta^2(\omega_0) \\ &= 2\bar\alpha_+(\omega_0)\bar\theta^\star - \bar\alpha_+^2(\omega_0) - \bar\beta^2(\omega_0) \end{aligned} \tag{87}$$

hold. Moreover, the derivative of $l(\bar\theta^\star)$ with respect to $\bar\alpha(\omega_0)$ evaluated at $\bar\alpha(\omega_0) = \bar\alpha_-(\omega_0)$ and $\bar\alpha(\omega_0) = \bar\alpha_+(\omega_0)$ is given by

$$\begin{aligned} \left.\frac{dl(\bar\theta^\star)}{d\alpha(\omega_0)}\right|_{\alpha(\omega_0)=\alpha_-(\omega_0)} &= 2(\bar\theta^\star - \bar\alpha_-(\omega_0)) \\ &= 2\sqrt{|\bar\beta(\omega_0)|}\sqrt{1-|\bar\beta(\omega_0)|} \end{aligned} \tag{88}$$

and

$$\left.\frac{dl(\bar{\theta}^\star)}{d\alpha(\omega_0)}\right|_{\alpha(\omega_0)=\alpha_+(\omega_0)} = 2(\bar{\theta}^\star - \bar{\alpha}_+(\omega_0)) = -2\sqrt{|\bar{\beta}(\omega_0)|}\sqrt{1-|\bar{\beta}(\omega_0)|}\ , \tag{89}$$

respectively. As a consequence, $l(\bar{\theta}^\star)$ increases if $\alpha(\omega_0)$ is greater than $\alpha_-(\omega_0)$ and smaller than $\alpha_+(\omega_0)$, i.e., we have the relations

$$l(\bar{\theta}^\star) > f(\bar{\theta}^\star) \quad \text{if} \quad \alpha(\omega_0) > \alpha_-(\omega_0)$$

and

$$l(\bar{\theta}^\star) > f(\bar{\theta}^\star) \quad \text{if} \quad \alpha(\omega_0) < \alpha_+(\omega_0)\ .$$

Taking into account that, for any given $\bar{\beta}(\omega_0) \neq 0$, $f(\bar{\theta})$ and $l(\bar{\theta})$ have no intersections for $\alpha(\omega_0) = 0$ and $\alpha(\omega_0) = +\infty$ and that, by varying $\alpha(\omega_0)$, intersections can appear/disappear only if a tangency condition happens, the above relations imply that there exist two intersections if and only if $\alpha(\omega_0) \in [\alpha_-(\omega_0), \alpha_+(\omega_0)]$, thus concluding the proof. □

From the proof of Proposition 5 it is clear that the set $\mathcal{S}_{\omega_0}$ either it is empty or it is composed of two half straight lines. This allows for the following analytical characterization of the PPD bifurcation manifold $\mathcal{M}_{X_0,M}$.

**Proposition 6** *Let condition* (83) *hold. Then*

$$\mathcal{M}_{X_0,M} = \mathcal{M}^{(1)}_{X_0,M} \cup \mathcal{M}^{(2)}_{X_0,M} \tag{90}$$

*where* $\mathcal{M}^{(i)}_{X_0,M}$, $i = 1, 2$, *are given by*

$$\mathcal{M}^{(i)}_{X_0,M} = \Big\{(X_0, M):\ X_0 = X_0^{(i)}(\lambda)\ , \quad M = M^{(i)}(\lambda),\ \lambda > 0\Big\}\ , \tag{91}$$

*with*

$$X_0^{(i)}(\lambda) = \frac{1}{L_3(0)}\left(1 + L_1(0)m_0 - \left((1 + L_1(0)m_0)\cos\bar{\theta}_i + L_1(0)\frac{m_1 - m_0}{\pi}\left(\bar{\theta}_i\cos\bar{\theta}_i - \sin\bar{\theta}_i\right)\right)\lambda\right) \tag{92}$$

$$M^{(i)}(\lambda) = \frac{1}{|L_2(\jmath\omega_0)|}\left|1 + L_1(\jmath\omega_0)\left(m_0 - \frac{m_1 - m_0}{\pi}\left(\cos\bar{\theta}_i\sin\bar{\theta}_i - \bar{\theta}_i\right)\right)\right|\lambda\ . \tag{93}$$

*Proof.* Observe that the couples $(A, B) \in \mathcal{S}_{\omega_0}$ can be parameterized as $A = 1 - \lambda\cos\bar{\theta}_i$, $B = \lambda$ with $\lambda > 0$ and $\bar{\theta}_i$, $i = 1, 2$, solutions of (82). Hence, the proof directly follows once the expressions of $N_0$ and $N_1$ in (74) and (75) are computed according to this parameterization and substituted into (34) and (35). □

*Remark 10* Observe that the PPD bifurcation manifolds $\mathcal{M}^{(i)}_{X_0,M}$, $i = 1, 2$, are half straight lines. Their existence is ensured by condition (83) which has a simple geometrical interpretation in the complex plane (see Fig. 4.b). Indeed, if we consider the region of the complex plane

$$S_{pwl} = \Big\{s \in \mathbb{C}:\ \Big|\mathrm{Re}[s] - \arcsin\sqrt{|\mathrm{Im}[s]|}\Big| \leq \sqrt{|\mathrm{Im}[s]|}\sqrt{1-|\mathrm{Im}[s]|},\quad |\mathrm{Im}[s]| \leq 1\Big\}\ , \tag{94}$$

then (83) is satisfied if and only if

$$-\frac{\pi}{m_1 - m_0}\left(L_1^{-1}\left(\jmath\frac{\omega_0}{2}\right) + m_0\right) \in S_{pwl}\ , \tag{95}$$

which only depends on the constants $m_0$ and $m_1$ of the PWL nonlinearity and on the complex value of $L_1(s)$ at $s = \jmath\omega_0/2$. Also, the accuracy at any point $\lambda$ of $\mathcal{M}^{(i)}_{X_0,M}$, $i = 1, 2$, can be evaluated by computing the corresponding value of $D(A(\lambda), B(\lambda), \omega_0)$ via (39).

*Remark 11* If we consider the symmetric case of the PWL nonlinearity (73), i.e.,

$$n(y) = \begin{cases} -m_0 + m_1(y+1) & \text{if} \quad y < -1 \\ m_0 y & \text{if} \quad -1 \leq y \leq 1 \\ m_0 + m_1(y-1) & \text{if} \quad y > 1 \end{cases}\ , \tag{96}$$

it turns out that the PPSs can also be symmetric and can contain inside their range either both the points $y = 1$ and $y = -1$ or a single point. In particular, in the latter case the PPSs containing only $y = 1$ (i.e., $A - B \geq -1$) are exactly those found previously for the nonlinearity (73). Clearly, due to the symmetry the PPSs containing only $y = -1$ can be obtained by simply replacing $A$ with $-A$. Along this line, we can characterize the PPD bifurcation manifolds related to PPSs containing inside their range a single point only. Indeed, if condition 83 holds, then $\mathcal{M}_{X_0,M}$ is as in (90) once

$$\mathcal{M}^{(i)}_{X_0,M} = \left\{(X_0, M):\ X_0 = \pm|X_0^{(i)}(\lambda)|\ , \quad M = M^{(i)}(\lambda),\ \lambda \in \left(0, \frac{2}{1+\cos\bar{\theta}_i}\right]\right\}\ , \tag{97}$$

and $X_0^{(i)}(\lambda)$ and $M^{(i)}(\lambda)$, $i = 1, 2$, are as in (92) and (93), respectively. The $\pm$ sign is due to the symmetry of the nonlinearity (96) which implies that for any given $\lambda$ there exist four PPSs with $A = \pm(1 - \lambda\cos\bar{\theta}_i)$ and $B = \lambda$, $i = 1, 2$, which undergo to a PPD bifurcation.
To complete the PPD bifurcation manifold in this symmetric case, we need to consider also PPSs including both the points $y = 1$ and $y = -1$. In this case we can resort to Proposition 2, thus computing the set $\mathcal{S}_{\omega_0}$ according to (49) along with the constraint $A - B \leq -1$ and then using (51).

*Remark 12* Section 4 and its Subsections 4.1 and 4.2 provide systematic procedures to compute PPSs and PPD manifolds for linear-plus-cubic and PWL nonlinearities, respectively. For the linear-plus-cubic case, the procedure can be summarized as follows.

i For a given forcing input of frequency $\omega_0$, check the graphical condition (71) to assess if the PPD manifold $\mathcal{M}_{X_0,M}$ is not empty, i.e., if there exist PPSs which undergo a period doubling bifurcation.
ii Use (67) to compute the offset and amplitude couples $(A, B)$ of the PPSs to which a PPD bifurcation pertains.
iii Use (68) and (69) to determine all the amplitudes $M$ of the forcing term, and the constant inputs $X_0$ characterizing the PPD bifurcation manifold $\mathcal{M}_{X_0,M}$.
iv Use (72) to compute the distortion index for evaluating the accuracy of the PPD bifurcation manifold $\mathcal{M}_{X_0,M}$.

The PWL case can be approached similarly by using the graphical condition (95) in place of (71) and formulas (92) and (93) in place of (68) and (69). It is worth stressing that with respect to standard continuation techniques, which rely on heavy numerical computations (see [50] and references within), the proposed procedures allow one to predict period doubling bifurcations of periodic solutions of frequency $\omega_0$, by using closed form formulas.

## 5 Numerical examples

In this section we focus on the memristor circuit of Fig. 2 as a vehicle to illustrate the results of Section 4. As already said, the circuit is known to show a rich dynamics as the amplitude and the frequency of the harmonic voltage input $u$ are varied and the initial conditions are properly chosen.
Proposition 1 guarantees that the circuit dynamics is described by the input-output relation (1), once $y = \varphi_M$, $\tau = t$ and the rational functions $L_i(\mathcal{D})$, $i = 1, 2, 3$, the nonlinearity $n(\cdot)$, the harmonic signal amplitude $M$, frequency $\omega_0$, phase $\theta_0$, the constant input $\mathrm{X}_0$ are as in (8), (9), (10), (11), respectively.
The aim is to compute for a given frequency $\omega_0$ the PPD bifurcation manifold $\mathcal{M}_{X_0,M}$ for both nonlinearities (52) and (73) according to the procedure presented in Remark 12. Also, the accuracy of these predicted manifolds is evaluated by computing numerically the distortion index and by comparing $\mathcal{M}_{X_0,M}$ with the true period doubling bifurcation manifold.
The development of the next subsections should make it clear that similar conclusions can be also drawn for other memristor circuits, as the ones reported in Table 1.

### 5.1 Linear plus cubic nonlinearity

In the case of nonlinearity (52), the manifold $\mathcal{M}_{X_0,M}$ is not empty if and only if condition (71) of Remark 8 holds. Hence, according to point (i) of Remark 12, for the memristor circuit of Fig. 2 we get

$$-\frac{\left(1 - LC\frac{\omega_0^2}{4} + m_0 R\right) + \jmath\frac{\omega_0}{2}\left(RC + m_0 L\right)}{m_1\left(R + \jmath L\frac{\omega_0}{2}\right)} \in S_{lc} \ . \tag{98}$$

Observe that this condition provides quite a simple characterization of the values of the circuit parameters for which $\mathcal{S}_{\omega_0}$ and hence $\mathcal{M}_{X_0,M}$ are not empty. Also, since the left hand side term of (98) depends continuously on the system parameters, it turns out that $\mathcal{M}_{X_0,M}$ enjoys a robustness property, in the sense that it is not destroyed for small variations of the circuit parameters. Once the circuit parameters satisfy this condition, the PPD bifurcation manifold $\mathcal{M}_{X_0,M}$ can be analytically computed exploiting Proposition 4 as explained in points (ii) and (iii) of Remark 12. To proceed, let us consider the following numerical values for the circuit parameters:

$$\begin{aligned} &R = 1,\ L = 1,\ C = 1, \\ &m_0 = -1.225,\ m_1 = 0.206,\ \hat{\theta} = 0 \ . \end{aligned} \tag{99}$$

By plotting the resulting left hand side term of (98) as a function of $\omega_0$, we get that the graphical condition is satisfied for all $\omega_0 \in (0, 2.698)$, as shown in Fig. 5. Let us consider the specific value of $\omega_0 = 1.2$ at which the left hand side term of 98 assumes the complex value $2.377 - \jmath\,0.771$ which is marked with $\star$ in Fig. 5. According to Proposition 4 and Remark 7, the two closed curves composing manifold $\mathcal{M}_{X_0,M}$ can be computed analytically for $\lambda \in [0, 2\pi)$.

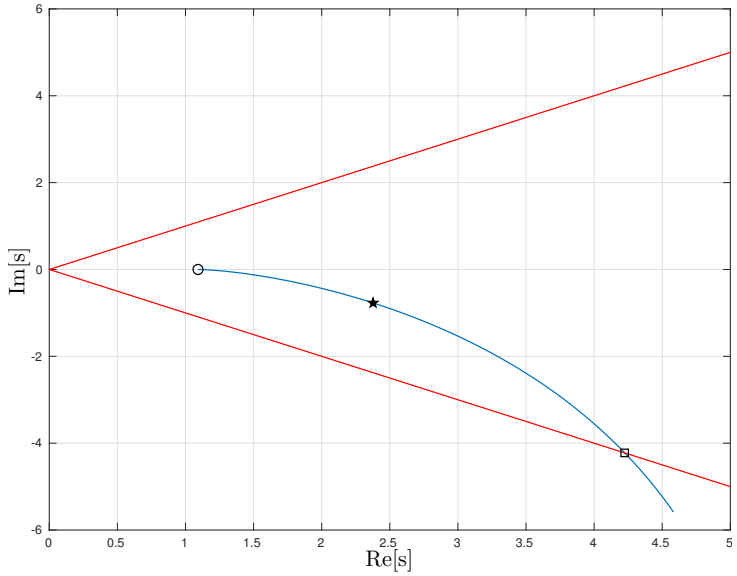


**Fig. 5** Graphical interpretation of condition (98) for varying $\omega_0$ (see also Fig. 4a). The circle correspond to $\omega_0 = 0$, while the square to $\omega_0 = 2.698$. The star relates to a chosen value of $\omega_0$ used to exemplify the PPD manifold in the $(X_0, M)$ space.

Figure 6 reports the closed curve (dashed line) corresponding to $-|A(\lambda)|$ (the one pertaining to $|A(\lambda)|$ is symmetric with respect to the $M$-axis) in the $(M, X_0)$-plane, where the points corresponding to $\lambda = 0$, $\pi/2$, $\pi$, $3\pi/2$ are denoted with the symbols $\circ, +, *, \diamondsuit$, respectively. Note that the bifurcations points can be obtained by fixing $X_0$ and varying $M$ or fixing $M$ and varying $X_0$. The first case corresponds to fix the initial conditions of the memristor circuits and varying the amplitude of the harmonic voltage input. More specifically, for $X_0 = 0$, PPD bifurcations occur at $M = 0.385$ and $M = 1.075$. The second case concerns to the so-called "bifurcations without parameters" since it corresponds to vary only the initial conditions of the circuit. For instance, if $M = 0.8$ (vertical straight line) then PPD bifurcations occur at $X_0 = -0.237$ and $X_0 = 0.027$. Remark 6 ensures that a bifurcated PPS pertain to each point $(X_0(\lambda), M(\lambda))$ of the closed curve, whose offset $-|A(\lambda)|$ and amplitude $B(\lambda)$ can be computed analytically according to (67). The accuracy of PPSs can be evaluated by computing the distortion index (72) which can be obtained as an analytical function $D(\lambda)$ for $\lambda \in [0, 2\pi)$. Figure 7 makes it possible to single out that $(3.03, 5.48)$ is the range of $\lambda$ to which correspond smaller values of $D(\lambda)$ (less than 0.05) and hence more reliable PPSs. Hence, it is expected that the PPD bifurcations points are more accurate in the part of the dashed closed curve of Fig. 6 which is comprised between the marks $*$ and $\diamondsuit$. This is indeed confirmed by the comparison in Fig. 6 where the true (numerically obtained by means of the Matlab continuation toolbox MatCont [50]) and PPD bifurcation curves are compared.

Finally, we observe that the PPD bifurcation curve can be used to locate more complex motions. Indeed, Fig. 8 reports the dynamical behaviors pertaining to the marked points on the vertical red line which correspond to different vaules of $X_0$, i.e., different initial conditions of the memristor circuit of Fig. 2 where $u(t) = 0.8\cos(1.2\,t)$ and the circuit parameters are as in (99). Similar complex behaviors can be obtained by considering nearby different points in the $(M, X_0)$-plane.

### 5.2 PWL nonlinearity

In the case of nonlinearity (73), condition (95) for non-empty $\mathcal{M}_{X_0,M}$ reduces to

$$-\frac{\pi\left(1 - LC\frac{\omega_0^2}{4} + m_0 R\right) + \jmath\frac{\pi\omega_0}{2}\left(RC + m_0 L\right)}{(m_1 - m_0)\left(R + \jmath L\frac{\omega_0}{2}\right)} \in S_{pwl}\ . \tag{100}$$

Let us now consider the following numerical values of the circuit parameters:

$$R = 1,\ L = 1,\ C = 1,$$
$$m_0 = -1.02,\ m_1 = -0.4,\ \hat{\theta} = 0\ . \tag{101}$$

It turns out that condition (100) is satisfied for all $\omega_0 \in (0.218, 1.269)$, as shown in Fig. 9. Let us consider the specific value of $\omega_0 = 1$ which yields the point marked with $\star$ in Fig. 9. According to Proposition 5 we get $\bar{\theta}_1 =$

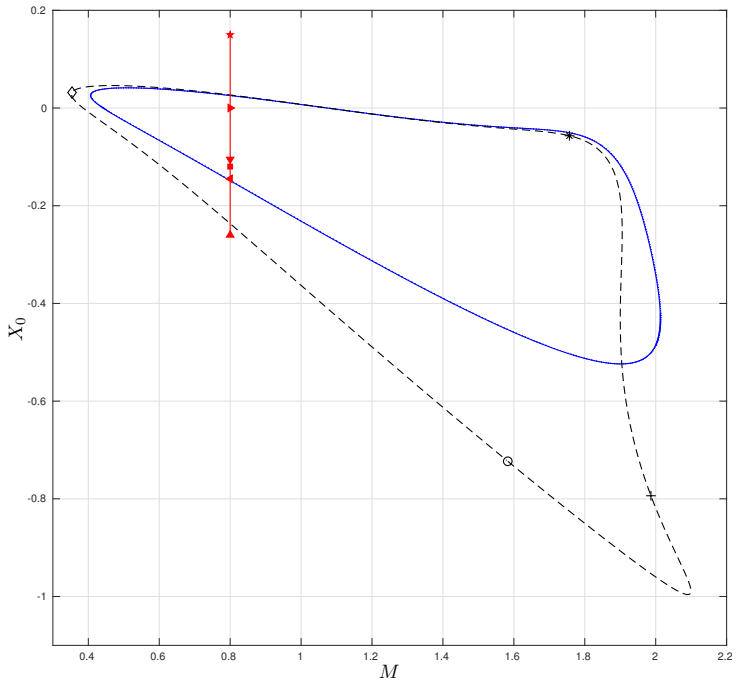


**Fig. 6** True (solid line) and predicted (dashed line) period doubling manifolds in the $(X_0, M)$ space corresponding to $\omega_0 = 1.2$. The manifolds are closed curve parametrized in $\lambda \in [0, 2\pi)$. The symbols $\circ, +, *, \diamondsuit$ are referred to $\lambda = 0, \pi/2, \pi, 3\pi/2$, respectively. The straight line for fixed $M = 0.8$ stands for the "bifurcation without parameters" path exemplified in Section 5.1, and the symbols on it are referred to the diagrams in next Fig. 8.

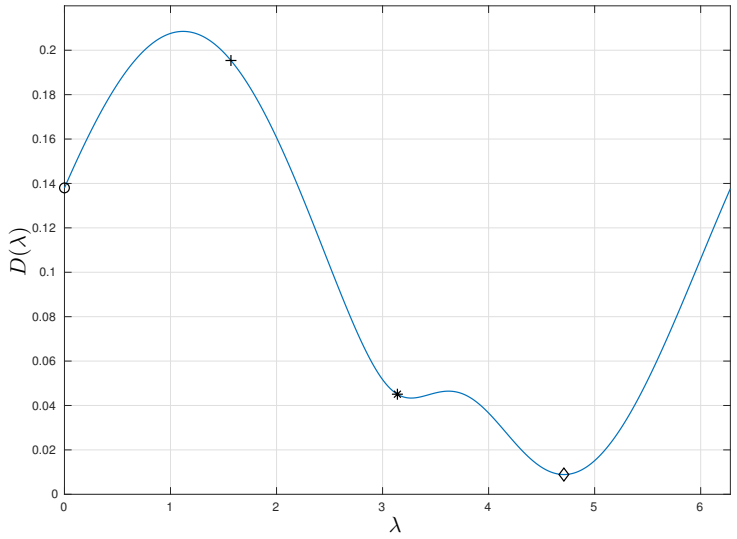


**Fig. 7** The distortion index (72) evaluated over parameter $\lambda$, namely $D(\lambda)$ for $\lambda \in [0, 2\pi]$, as explained in Remark 8. The symbols refer to the values of $\lambda$ illustrated in Fig. 6 at $\omega_0 = 1.2$.

0.708 and $\bar{\theta}_2 = 1.910$. Hence, Proposition 6 provides the PPD bifurcation manifold $\mathcal{M}_{X_0,M}$ which is composed of two straight half lines parametrically described by $\lambda \in (0, +\infty)$, according to (92)-(93).

Fig. 10 shows the PPD bifurcation manifold (dashed curve) together with the true one (solid curve), computed using MatCont toolbox and a smooth approximation of the PWL function [51]. Observe that the predictions are more accurate for the lower straight line and hence the PPSs are expected to be more reliable for this straight line. This is indeed confirmed by computing the distortion index $D^{(i)}(\lambda)$ for each point $(X_0^{(i)}(\lambda), M^{(i)}(\lambda))$ of the two straight lines by putting to $A = 1 - \lambda \cos \bar{\theta}_i$ and $B = \lambda$ in (39). Fig. 11 shows

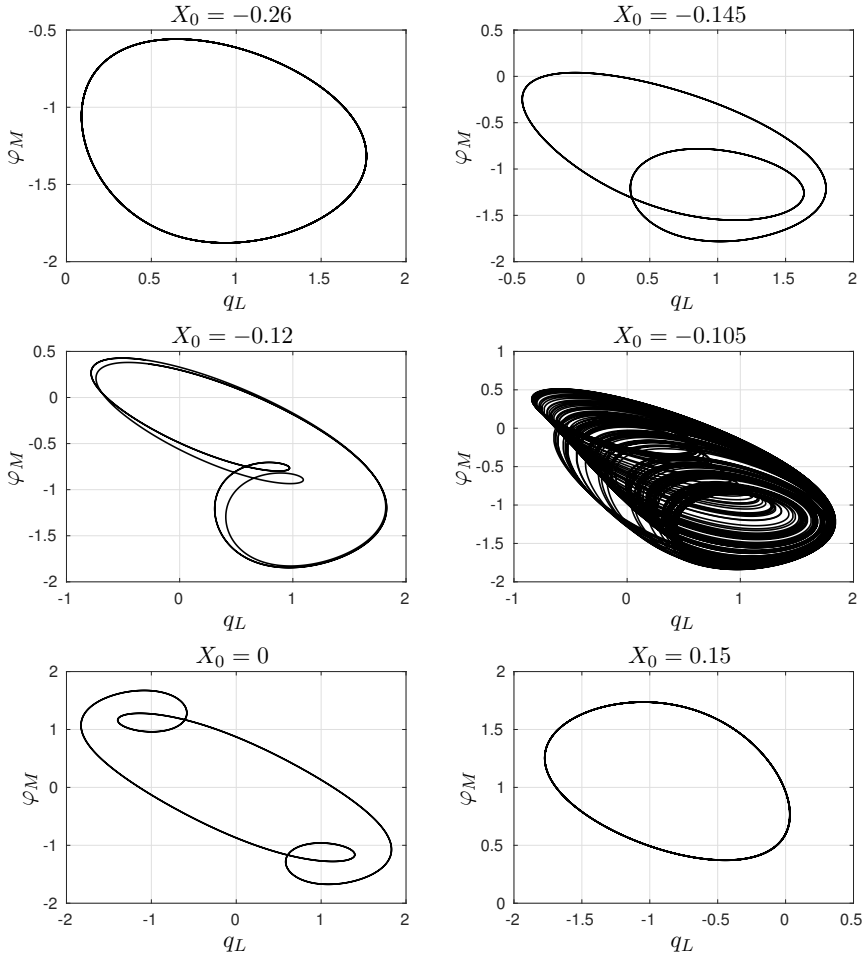


**Fig. 8** Dynamical behaviors along the vertical line ($M = 0.8$) of Fig. 6. From top-left to bottom-right: simple periodic solution for $X_0 = -0.26$ (point ▲ in Fig. 6); period-2 solution for $X_0 = -0.145$ (◀); period-4 solution for $X_0 = -0.12$ (■); chaotic solution for $X_0 = -0.105$ (▼); period-3 solution for $X_0 = 0$ (►) and another simple periodic solution for $X_0 = 0.15$ (★). The considered state variables are the inductor charge ($q_L$) and the memristor flux ($\varphi_M$).

$D^{(1)}(\lambda)$ and $D^{(2)}(\lambda)$ for the lower and upper straight lines of the PPD bifurcation manifold, respectively.

Finally, we can compute the PPD bifurcation manifold for the PWL symmetric nonlinearity (96) with $m_0 = -1.02$ and $m_1 = -0.4$ proceeding as described in Remark 11. Fig. 12 reports the closed curve corresponding to $|X_0^{(i)}(\lambda)|$ in (97) (the one pertaining to $-|X_0^{(i)}(\lambda)|$ is symmetric with respect to the $M$-axis) together with the true curve, showing quite a good accuracy also in the symmetric case.

## 6 Conclusions

This paper considers a class of memristor circuits which are known from simulations and experiments to display quite a rich dynamical behavior once the amplitude and the frequency of an external harmonic signal are varied. It is first shown that each circuit of the class admits an equivalent input-output representation in terms of a family of harmonically forced nonlinear feedback systems parameterized by an additional constant input which depends on the initial conditions of the memristor circuit. This property permits to clarify both the relation between classical nonlinear circuits and their memristor versions as well as the influence of memristor circuit initial conditions on its dynamical behavior. Successively, the input-output representation is investigated via the Harmonic Balance Method (HBM) to determine Predicted Periodic Solutions (PPSs) and their Predicted Period Doubling (PPD) bifurcations as the amplitude and frequency of the external harmonic signal and the additional constant input are varied. It is shown that for any given frequency the PPD bifurcation manifolds in the harmonic amplitude and constant input space can be readily computed. For the cases of linear-plus-cubic and PWL nonlinearities quite simple graphical tests are provided to compute the range of

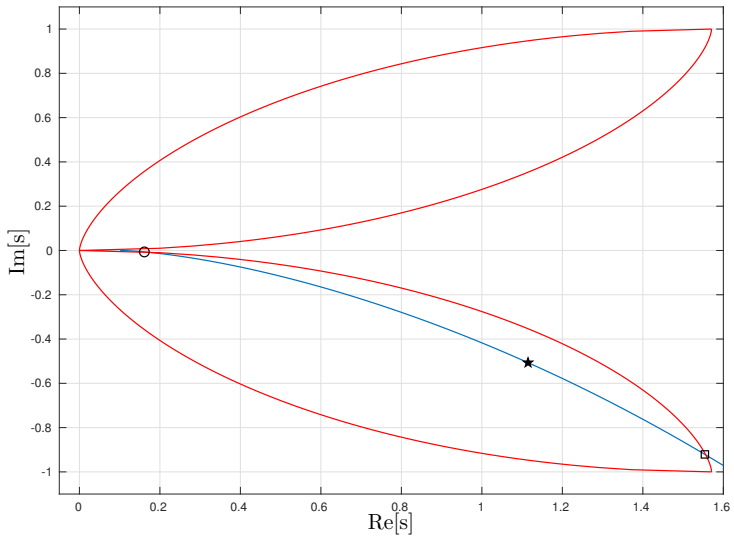


**Fig. 9** Graphical interpretation of condition (100) for varying $\omega_0$ (see also Fig. 4b). The circle correspond to $\omega_0 = 0.218$, while the square to $\omega_0 = 1.269$. The star relates to a chosen value of $\omega_0$ used to exemplify the PPD manifold in the $(X_0, M)$ space.

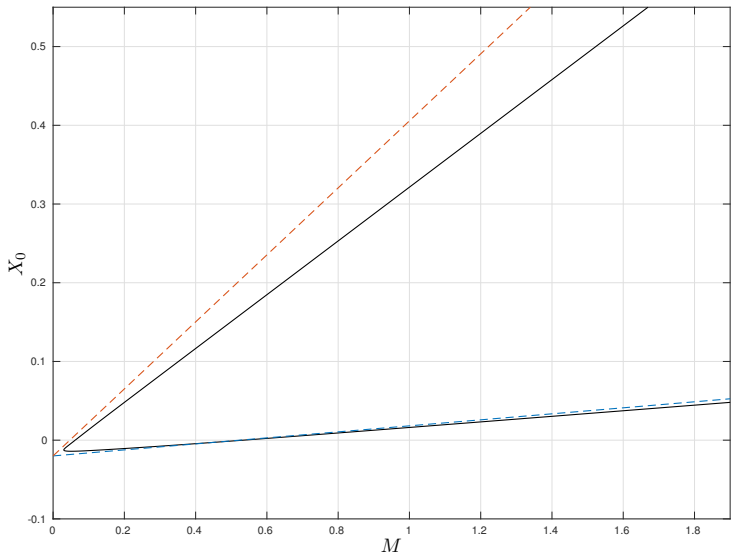


**Fig. 10** True (solid line) and predicted (dashed line) PPD manifolds in the $(X_0, M)$ space for asymmetric PWL nonlinearity at $\omega_0 = 1$. The lower dashed half line is obtained for $\bar{\theta}_1 = 0.708$, while the upper half for $\bar{\theta}_2 = 1.910$.

frequencies to which correspond non-empty PPD bifurcation manifolds. Moreover, it is shown that these predicted manifolds can be obtained in a closed form. Also, their accuracy can be evaluated by computing the distortion index pertaining to the related bifurcated PPSs. Finally, two numerical examples are presented to illustrate the proposed results and their effectiveness. It is also shown how the PPD bifurcation manifolds can be used to locate more complex dynamical behaviors.

## Conflict of Interest

The authors declare that they have no conflict of interest.

## Ethical approval

This article does not contain any studies with human participants or animals performed by any of the authors.

## Informed consent

Informed consent was obtained from all individual participants included in the study.

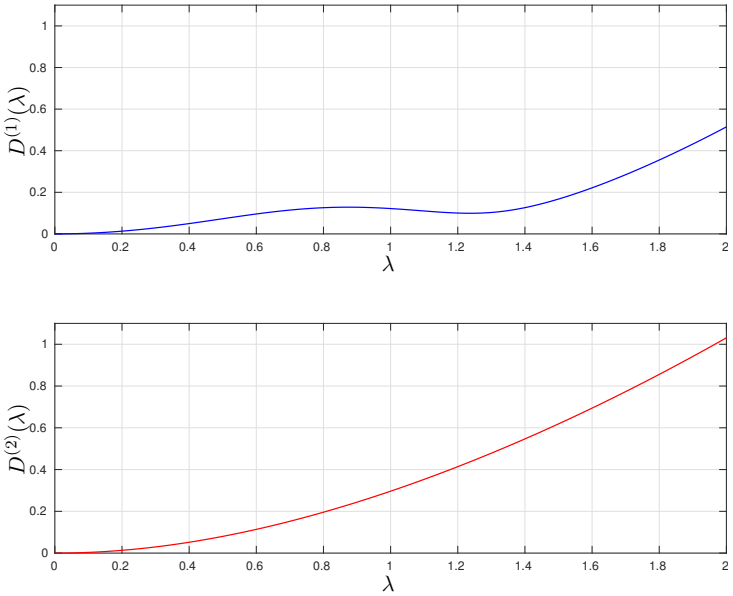


**Fig. 11** The distortion index (72) evaluated at $\omega_0 = 1$ over parameter $\lambda$, namely $D(\lambda)$ for $\lambda \in [0, 2\pi]$, as explained in Remark 8. Upper diagram: Distortion along the upper dashed line of Fig. 10. Lower diagram: Distortion along the lower dashed line of Fig. 10.

## References


1. L. O. Chua. Memristor-The missing circuit element. *IEEE Trans. Circuit Theory*, 18(5):507–519, Sep. 1971.
2. D. B. Strukov, G. S. Snider, D. R. Stewart, and R. S. Williams. The missing memristor found. *Nature*, 453(7191):80–83, May 2008.
3. P. Mazumder, S. M. Kang, and Waser, R. (Eds.). Special issue on memristors: devices, models, and applications. *Proc. IEEE*, 100(6), Jun. 2012.
4. R. Tetzlaff (Ed.). *Memristors and Memristive Systems*. Springer, New York, 2014.
5. A. Adamatzky and L. Chua (Eds.). *Memristor Networks*. Springer, New York, 2014.
6. F. L. Traversa and M. Di Ventra. Universal memcomputing machines. *IEEE Trans. Neural Netw. Learn. Syst.*, 26(11):2702–2715, 2015.
7. L. Chua. Everything you wish to know about memristors but are afraid to ask. *Radioengineering*, 24(2):319–368, 2015.
8. M. Itoh and L. O. Chua. Memristor oscillators. *Int. J. Bifurcat. Chaos*, 18(11):3183–3206, Nov. 2008.
9. S. Kumar, J. P. Strachan, and R. S. Williams. Chaotic dynamics in nanoscale NbO2 Mott memristors for analogue computing. *Nature*, 2017.
10. F. Corinto, A. Ascoli, and M. Gilli. Nonlinear dynamics of memristor oscillators. *IEEE Trans. Circuits Syst. I, Reg. Papers*, 58(6):1323–1336, Jun. 2011.
11. L. V. Gambuzza, A. Buscarino, L. Fortuna, and M. Frasca. Memristor-based adaptive coupling for consensus and synchronization. *IEEE Trans. Circuits Syst. I: Reg. Papers*, 62(4):1175–1184, Apr. 2015.
12. A. Ascoli, R. Tetzlaff, Z. Biolek, Z. Kolka, V. Biolkova, and D. Biolek. The art of finding accurate memristor model solutions. *IEEE J. Emerg. Select. Topics Circuits Syst.*, 5(2):133–142, Jun. 2015.
13. H. Kim, M. Sah, C. Yang, T. Roska, and L. O. Chua. Memristor bridge synapses. *Proc. IEEE*, 100(6):2061–2070, 2012.
14. S. Kvatinsky, M. Ramadan, E. G. Friedman, and A. Kolodny. VTEAM: A general model for voltage-controlled memristors. *IEEE Trans. Circuits Syst. II*, 62(8):786–790, 2015.
15. B. Muthuswamy. Implementing memristor based chaotic circuits. *Int. J. Bifurc. Chaos*, 20(05):1335–1350, 2010.
16. Q. Li, S. Hu, S. Tang, and G. Zeng. Hyperchaos and horseshoe in a 4D memristive system with a line of equilibria and its implementation. *Int. J. Circuit Theory Appl.*, 42(11):1172–1188, 2014.
17. M. C. Scarabello and M. Messias. Bifurcations leading to nonlinear oscillations in a 3D piecewise linear memristor oscillator. *Int. J. Bifurc. Chaos*, 24(1):1430001, 2014.
18. M. Messias, C. Nespoli, and V. A. Botta. Hopf bifurcation from lines of equilibria without parameters in memristor oscillators. *Int. J. Bifurcation Chaos*, 20(02):437–450, 2010.
19. B. Bao, T. Jiang, Q. Xu, M. Chen, H. Wu, and Y. Hu. Coexisting infinitely many attractors in active band-pass filter-based memristive circuit. *Nonlinear Dynamics*, 86(3):1711–1723, 2016.
20. E. Ponce, A. Amador, and J. Ros. A multiple focus-center-cycle bifurcation in 4d discontinuous piecewise linear memristor oscillators. *Nonlinear Dynamics*, Sep 2018.
21. F. Yuan, G. Wang, Y. Shen, and X. Wang. Coexisting attractors in a memcapacitor-based chaotic oscillator. *Nonlinear Dynamics*, 86(1):37–50, 2016.
22. K. Rajagopal, S. Jafari, A. Karthikeyan, A. Srinivasan, and B. Ayele. Hyperchaotic memcapacitor oscillator with infinite equilibria and coexisting attractors. *Circuits Syst. Signal Process.*, 37(9):3702–3724, Sep 2018.
23. F. Yuan, G. Wang, and X. Wang. Chaotic oscillator containing memcapacitor and meminductor and its dimensionality reduction analysis. *Chaos*, 27(3), 2017.
24. B. Xu and Y. Wang, G. Shen. A simple meminductor-based chaotic system with complicated dynamics. *Nonlinear Dynamics*, 88(3):2071–2089, May 2017.

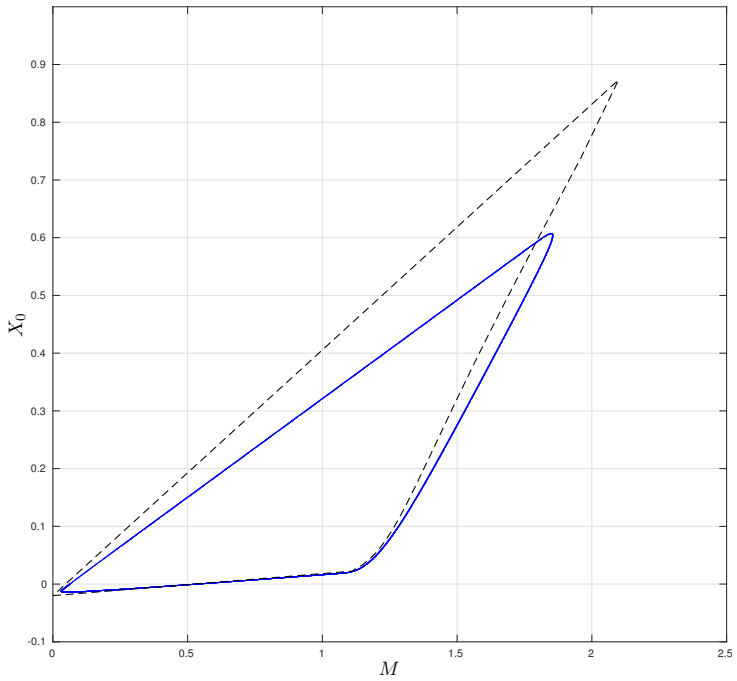


**Fig. 12** True (solid line) and predicted (dashed) bifurcation manifolds in the $(X_0, M)$ space for the symmetric PWL nonlinearity. Both predicted and true bifurcation manifolds are computed using a smooth approximation of the PWL functions and are evaluated numerically.


25. A. Amador, E. Freire, E. Ponce, and J. Ros. On discontinuous piecewise linear models for memristor oscillators. *Int. J. Bifurc. Chaos*, 27(06):1730022, 2017.
26. E. Ponce, J. Ros, E. Freire, and A. Amador. Unravelling the dynamical richness of 3d canonical memristor oscillators. *Microelectron. Eng.*, 182:15–24, 2017.
27. F. Corinto and M. Forti. Memristor circuits: Flux–charge analysis method. *IEEE Trans. Circuits Syst. I, Reg. Papers*, 63(1):1997–2009, Nov. 2016.
28. F. Corinto and M. Forti. Memristor circuits: Bifurcations without parameters. *IEEE Trans. Circuits Syst. I, Reg. Papers*, 64(6):1540–1551, 2017.
29. F. Corinto and M. Forti. Memristor circuits: Pulse programming via invariant manifolds. *IEEE Trans. Circuits Syst. I: Reg. Papers*, 65(4):1327–1339, 2018.
30. M. Di Marco, M. Forti, G. Innocenti, and A. Tesi. Harmonic balance method to analyze bifurcations in memristor oscillatory circuits. *Int. J. Circuit Theory Appl.*, 46:66–83, Jan. 2018.
31. D. P. Atherton. *Nonlinear Control Engineering*. Van Nostrand Reinhold, London, 1975.
32. A. I. Mees. *Dynamics of Feedback Systems*. Wiley, New York, 1981.
33. H. K. Khalil. *Nonlinear systems (3rd edition)*. Prentice-Hall, Upple Saddle River, New Jersey, 2002.
34. A. I. Ahamed and M. Lakshmanan. Discontinuity induced Hopf and Neimark–Sacker bifurcations in a memristive Murali–Lakshmanan–Chua circuit. *Int. J. Bifurcat. Chaos*, 27(06):1730021, 2017.
35. Q. Xu, Q. Zhang, B. Bao, and Y. Hu. Non-autonomous second-order memristive chaotic circuit. *IEEE Access*, 5:21039–21045, 2017.
36. B. Bao, P. Jiang, H. Wu, and F. Hu. Complex transient dynamics in periodically forced memristive Chua's circuit. *Nonlinear Dynamics*, 79(4):2333–2343, 2015.
37. A. I. Ahamed and M. Lakshmanan. Nonsmooth bifurcations, transient hyperchaos and hyperchaotic beats in a memristive Murali–Lakshmanan–Chua circuit. *Int. J. Bifurcat. Chaos*, 23(06):1350098, 2013.
38. A. Buscarino, L. Fortuna, M. Frasca, and L. V. Gambuzza. A new driven memristive chaotic circuit. In *2013 European Conference on Circuit Theory and Design (ECCTD)*, pages 1–4, 2013.
39. K. Murali, M. Lakshmanan, and L. O. Chua. The simplest dissipative nonautonomous chaotic circuit. *IEEE Trans. Circuits Syst. I*, 41(6):462–463, 1994.
40. R. Genesio and A. Tesi. Harmonic balance methods for the analysis of chaotic dynamics in nonlinear systems. *Automatica*, 28(3):531–548, 1992.
41. C. Piccardi. Bifurcations of limit cycles in periodically forced nonlinear systems: The harmonic balance approach. *IEEE Trans. Circuits Syst. I*, 41(12):315–320, 1994.
42. A. Tesi, E. H. Abed, R. Genesio, and H. O. Wang. Harmonic balance analysis of period-doubling bifurcations with implications for control of nonlinear dynamics. *Automatica*, 32(9):1255–1271, 1996.
43. M. Basso, R. Genesio, and A. Tesi. A frequency method or predicting limit cycle bifurcations. *Nonlinear Dynamics*, 13:339–360, 1997.
44. F. Bonani and M. Gilli. Analysis of stability and bifurcations of limit cycles in Chua's circuit through the harmonic-balance approach. *IEEE Trans. Circuits Syst. I*, 46:881–890, 1999.
45. M. Di Marco, M. Forti, and A. Tesi. Harmonic balance approach to predict period-doubling bifurcations in nearly-symmetric neural networks. *J. Circuits Syst. Computers*, 12(4):435–460, Jul. 2003.
46. G. Innocenti, A. Tesi, and R. Genesio. Complex behaviour analysis in quadratic jerk systems via frequency domain Hopf bifurcation. *Int. J. Bifurc. Chaos*, 20(3):657–667, 2010.

47. Y. Lu, X. Huang, S. He, D. Wang, and B. Zhang. Memristor based van der Pol oscillation circuit. *Int. J. Bifurcat. Chaos*, 24(12):1450154, 2014.
48. Z. Galias. Study of amplitude control and dynamical behaviors of a memristive band pass filter circuit. *IEEE Trans. Circuits Syst. II*, 65(5):637–641, 2018.
49. K.J. Chandía, M. Bologna, and B. Tellini. Multiple scale approach to dynamics of an LC circuit with a charge-controlled memristor. *IEEE Trans. Circuits Syst. II*, 65(1):120–124, Jan 2018.
50. A. Dhooge, W. Govaerts, and Y. A. Kuznetsov. MATCONT: a MATLAB package for numerical bifurcation analysis of ODEs. *ACM Trans. on Math. Software (TOMS)*, 29(2):141–164, 2003.
51. V.M. Jimenez-Fernandez, M. Jimenez-Fernandez, H. Vazquez-Leal, E. Muñoz Aguirre, H.H. Cerecedo-Nuñez, U.A. Filobello-Niño, and F.J. Castro-Gonzalez. Transforming the canonical piecewise-linear model into a smooth-piecewise representation. *SpringerPlus*, 5(1), 2016.